

# Compliance-based topology optimization of structural components subjected to thermo-mechanical loading

Ticho Ooms<sup>1\*</sup> (0000-0001-5140-6113), Gieljan Vantghem<sup>1,2</sup> (0000-0002-7265-9782), Thomas Thienpont<sup>1</sup> (0000-0003-1466-3377), Ruben Van Coile<sup>1</sup> (0000-0002-9715-6786), Wouter De Corte<sup>1</sup> (0000-0002-9416-3593)

<sup>1</sup>Department of Structural Engineering and Building Materials, Ghent University, Technologiepark-Zwijnaarde 60, Zwijnaarde 9052, Belgium

<sup>2</sup>Concrenetics, Rue des Sablières 16, Tournai 7522, Belgium

\*Corresponding author: [Ticho.Ooms@UGent.be](mailto:Ticho.Ooms@UGent.be)

## Abstract

Apart from mechanical actions, structural components in the construction industry may be subjected to a thermal gradient, causing (internally) restrained thermal expansion. These thermal loads can alter the mechanical response of components in a structural topology optimization procedure. Therefore, the influence of thermal loading should be considered in the sensitivity analysis to efficiently update the structural layout of material. In this paper, a density-based topology optimization procedure is developed for compliance minimization of structural components subjected to thermo-mechanical loads considering steady-state heat conduction and weak thermo-mechanical coupling. The adjoint method is employed to obtain the analytical sensitivities, taking into account the influence of the design-dependent temperature field and thermal properties. The proposed topology optimization procedure is demonstrated on the MBB problem, extended with thermal loading, to investigate the influence of the proposed sensitivities on the optimized results. Furthermore, the thermo-mechanical load ratio is quantitatively defined and its effect on the resulting topologies is studied. The results show that the thermo-mechanical load ratio significantly changes the topology of the optimized results. Finally, the topology optimization procedure is presented in an efficient 138-line MATLAB code and provided as supplementary material, serving as a basis for further research.

## Keywords

Topology optimization, structural components, thermo-mechanical loading, steady-state heat conduction, heat transfer

## 1 Introduction

In the construction industry, the production of cement for concrete structures plays a significant part in the global CO<sub>2</sub> emissions (Andrew, 2018; Stoiber & Kromoser, 2021). This problem can be addressed by either decreasing the amount of cement in concrete mixtures on a material level or reducing the amount of material in construction elements on a structural level, e.g. through structural optimization (Stoiber & Kromoser, 2021). The most general approach to structural optimization is topology optimization (TO). This mathematical technique allows for the optimization of the material layout within a certain design space, given a set of boundary conditions, loads and constraints, and without the requirement of an a priori arbitrary guess for the final design. Therefore, topology optimization can offer inspiration for more efficient design solutions for building components or structures.

Many topology optimization examples from literature strictly use externally applied, constant mechanical loads with regard to structural optimization problems (Bourdin & Chambolle, 2003). Even though a structural component in the construction industry is typically designed with three mechanical requirements in mind (i.e. stiffness, strength and stability), these are not solely challenged by mechanical actions on the structure. A common

example of such a non-mechanical action is thermal loading caused by environmental temperature changes or exposure to fire. In essence, thermal loading may cause thermo-mechanical stress in a structure. As a result of a changing temperature field in the structure that is determined by a heat transfer analysis, (internally) restrained thermal expansion causes internal forces and stresses. When the material distribution changes during the optimization process, the temperature field needs to be recalculated and the corresponding thermo-mechanical loads will change accordingly. Hence, thermal loading is an example of so-called design-dependent loads, i.e. loads of which the magnitude, direction and location are dependent on the material layout itself and which are subject to change in each iteration in the optimization process (Bourdin & Chambolle, 2003; Chen & Kikuchi, 2001). Other common examples of design-dependent loads are self-weight (Bruyneel & Duysinx, 2005; Huang & Xie, 2011) and pressure loads (Hammer & Olhoff, 2000; Lee & Martins, 2012; Picelli et al., 2015, 2019; Zheng et al., 2009) among others. A clear overview of different types of design-dependent loads, in particular thermal loading, is given by Gao and Zhang (2010).

Thermo-mechanical loading in topology optimization, also often called thermo-elastic topology optimization, has already been studied since the seminal paper from Rodrigues and Fernandes (1995), in which they used the homogenization method for compliance-based problems. Later, Li et al. (2001) studied the effects of varying temperature fields and Diaz and Benard (2003) investigated the optimization of heat-resistant structures. Gao and Zhang (2010) discussed the design-dependency of thermal loads and proposed the use of a thermal stress coefficient (TSC) for the penalization related to the thermal expansion. Li et al. (2010) applied the evolutionary structural optimization (ESO) method with displacement minimization to the design of thermo-elastic structures in and Zhu et al. (Zhu et al., 2019) proposed a procedure for temperature-constrained TO with thermo-mechanical loads, considering steady-state heat conduction (SHC) and thermally induced stresses due to thermal expansion. Other sources studied either compliance-based (Gao & Zhang, 2010) or stress-based (Deaton & Grandhi, 2013; Hou et al., 2016) approaches for thermo-mechanical loading. Further, multi-material TO with thermo-mechanical loading has been explored (Chen et al., 2022; Chen et al., 2021; Gao et al., 2016; Giraldo-Londoño et al., 2020) and simultaneous optimization of stiffness and thermal properties has been investigated (Diaz & Benard, 2003; Ganobjak & Carstensen, 2019; Vantighem et al., 2019) as well, although the latter should not necessarily be considered design-dependent thermal loading. An extensive overview of thermal loading in TO is provided by Deaton and Grandhi (Deaton & Grandhi, 2014) with a more recent update by Leader (Leader, 2021).

Several studies have confirmed that the results of a TO procedure considering thermo-mechanical loading are significantly influenced by the thermal loads (Cho & Choi, 2005; Diaz & Benard, 2003). Hence, the thermal contribution and its design-dependency needs to be taken into account in the sensitivity analysis when gradient-based TO is used. Nevertheless, the influence of the design variables on the design-dependent temperature field is often neglected in the calculation of the sensitivities (Gao & Zhang, 2010; Gonçalves et al., 2022; Xia & Wang, 2008). This simplification is generally justified by the computational efficiency and the marginal influence on the optimized results. However, for thermally dominant problems, where the contribution of the thermal loading to the objective is far greater than its mechanical counterpart, this simplification could lead to inaccurate results and lack of convergence (Ooms et al., 2022), which is also addressed in this study. In a recent investigation, Zhu et al. (Zhu et al., 2019) have included the influence of the design variables on the temperature field and thermal stiffness matrix by means of the direct method for the sensitivity analysis. However, this leads to a computationally expensive calculation of the sensitivities. Hence, a more efficient approach is proposed by taking advantage of the adjoint method.

In this paper, the authors present a compliance-based topology optimization procedure for structures subjected to thermo-mechanical loading considering steady-state heat conduction. The sensitivity analysis is performed using the adjoint (variable) method, which allows for an efficient implementation of the TO procedure and solving large-scale thermo-mechanical optimization problems on a desktop computer with a reasonable computation time. A compact and easy to understand 138-line MATLAB code for 2D compliance minimization problems is provided as supplementary material, serving as a basis for further research. The remainder of this paper is organized as

follows. The theoretical background of the thermo-mechanical model and the topology optimization formulation (including sensitivity analysis) are provided in Section 2. Subsequently, the implementation of the thermo-mechanical model and the sensitivity analysis is described in Section 3, with references to the provided code. Finally, in Section 4 a numerical example of the MBB beam, extended with thermal loading, is solved using the developed TO procedure, followed by a parameter study and a discussion of the results thereof.

## 2 Thermo-elastic topology optimization

### 2.1 Governing equations

In this section, the governing state equations are derived for the thermal and mechanical analysis. In addition, the thermo-mechanical coupling is described.

#### 2.1.1 Thermal analysis

In this study, the thermal response of the structure is governed by heat conduction, as described by Fourier's law. The governing equation for steady-state heat conduction is then expressed in Eq. (1), based on the energy equation for a solid medium without fluid motion and under the assumption of steady-state heat transfer (Welty et al., 2014).

$$\kappa \nabla^2 \mathbf{T} + \mathbf{Q} = 0 \quad (1)$$

where  $\kappa$  is the thermal conductivity for isotropic materials,  $\nabla$  is the nabla operator and  $\mathbf{Q}$  is the internal volumetric heat generation and  $\mathbf{T}$  the temperature field, which is spatially varying and temporally constant.

As the governing equation for SHC in Eq. (1) is a second-order partial differential equation in the spatial domain, this requires two boundary conditions (BCs) in order to solve for the unknown temperatures in  $\mathbf{T}$ . Generally, there are two common types of BCs for heat conduction problems (expressed in Eq. (2)): an essential or Dirichlet condition, where a temperature  $T_a$  is specified on the boundary  $\Gamma_D$ , and a natural or Neumann condition, where a (normal) heat flux  $q$  is imposed on the boundary  $\Gamma_N$ , illustrated in Figure 1. In this study, Dirichlet conditions are considered for the thermal loading and Neumann conditions for adiabatic boundaries.

$$\begin{aligned} \mathbf{T} &= T_a \text{ on } \Gamma_D \in \Gamma \\ q &= -\kappa \frac{\partial \mathbf{T}}{\partial n} \text{ on } \Gamma_N \in \Gamma \end{aligned} \quad (2)$$

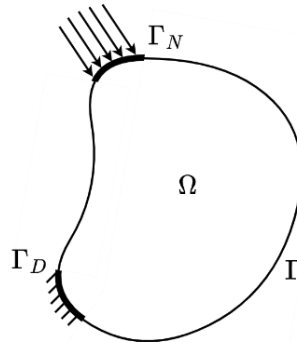


Figure 1: Boundary conditions

The governing equation for the thermal problem is first transformed into finite element equations. Different approaches exist to derive these equations, the reader is referred to (Lewis et al., 2004; Logan, 2016; Reddy &

Gartling, 2010). The finite element model (FEM) in matrix formulation for a thermal problem considering SHC is given by Eq. (3).

$$\mathbf{K}_{th}\mathbf{T} = \mathbf{Q} \quad (3)$$

where  $\mathbf{K}_{th}$  is the thermal stiffness matrix (named after its mechanical equivalent, see further),  $\mathbf{T}$  is the temperature field and  $\mathbf{Q}$  is the heat load vector. As Eq. (3) represents the global system of all finite elements,  $\mathbf{K}_{th}$  is assembled from the element thermal stiffness matrices as  $\mathbf{K}_{th} = \sum_e^{N_e} \mathbf{K}_{th}^e$ , wherein  $\sum_e^{N_e}$  is the assembly operator rather than a summation symbol and  $N_e$  is the number of elements.

The element thermal stiffness matrix  $\mathbf{K}_{th}^e$  is defined in Eq. (4) for 2D problems considering square elements, as it directly follows from the derivation of the FEM equation.

$$\mathbf{K}_{th}^e = \int_{\Omega_e} \mathbf{B}_{th}^T \mathbf{D}_{th} \mathbf{B}_{th} d\Omega = \iint_{\Omega_e} \mathbf{B}_{th}^T \mathbf{D}_{th} \mathbf{B}_{th} t dx dy \quad (4)$$

where  $\Omega_e$  is the element domain,  $t$  is the out-of-plane thickness,  $\mathbf{B}_{th}$  is the thermal gradient-temperature matrix and  $\mathbf{D}_{th}$  is the thermal conductivity matrix.

The thermal conductivity matrix  $\mathbf{D}_{th}$  is also known as the heat flux-thermal gradient relationship  $\kappa$  from Fourier's law, which contains the thermal conductive properties of the material in different dimensions. In Eq. (5) the thermal conductivity matrix is given for 2D heat conduction considering an isotropic material.

$$\mathbf{D}_{th} = \kappa \mathbf{D}_{th}^0 = \kappa \mathbf{I}_2 \quad (5)$$

where  $\mathbf{D}_{th}^0$  is the constant thermal conductivity matrix and  $\mathbf{I}_2$  is the identity matrix of size 2.

## 2.1.2 Mechanical analysis

The static, mechanical response of a structure is governed by Eq. (6), defining the equilibrium in a structure with a set of Dirichlet conditions (fixed displacements  $\mathbf{u}_0$ ) on  $\Gamma_D$  and Neumann conditions (known surface loads  $\mathbf{t}_0$ ) on  $\Gamma_N$  (see Figure 1).

$$\begin{aligned} \nabla^T \boldsymbol{\sigma} + \mathbf{b} &= 0 \\ \mathbf{u} &= \mathbf{u}_0 \quad \text{on } \Gamma_D \in \Gamma \\ \mathbf{t} &= \mathbf{t}_0 \quad \text{on } \Gamma_N \in \Gamma \end{aligned} \quad (6)$$

where  $\boldsymbol{\sigma}$  is the stress tensor,  $\mathbf{b}$  is the body force vector,  $\mathbf{u}$  is the displacement vector,  $\mathbf{t}$  the traction stress tensor. In this study, body forces such as self-weight are disregarded.

The linear strain-displacement relationship, assuming small deformations, is governed by Eq. (7).

$$\boldsymbol{\varepsilon} = \frac{1}{2} (\nabla \mathbf{u} + (\nabla \mathbf{u})^T) \quad (7)$$

where  $\boldsymbol{\varepsilon}$  is the (infinitesimal) strain tensor and superscript  $T$  denotes the transpose of a matrix.

Furthermore, the constitutive stress-strain relationship for linear-elastic and isotropic materials (Hooke's law) is formulated in Eq. (8).

$$\boldsymbol{\sigma} = \mathbf{D}(\boldsymbol{\varepsilon} - \boldsymbol{\varepsilon}_{th}) \quad (8)$$

where  $\mathbf{D}$  is the elasticity matrix for an isotropic material and  $\boldsymbol{\varepsilon}_{th}$  is the initial or thermal strain tensor in case of (weak) thermo-mechanical coupling (see further). Assuming 2D plane stress, matrix  $\mathbf{D}$  can be expressed in Eq. (9) in terms of the Young's modulus  $E$  and Poisson's ratio  $\nu$  as the elastic constants.

$$\mathbf{D} = E\mathbf{D}^0 = \frac{E}{1-\nu^2} \begin{bmatrix} 1 & \nu & 0 \\ \nu & 1 & 0 \\ 0 & 0 & \frac{1-\nu}{2} \end{bmatrix} \quad (9)$$

where  $\mathbf{D}^0$  is the constant elasticity matrix.

Similar to the thermal analysis, the governing equations from Eqs. (6), (7) and (8) can be further derived to the finite element equations according to (Zienkiewicz et al., 2013) until the global matrix notation for a static mechanical analysis is obtained in Eq. (10).

$$\mathbf{K}\mathbf{U} = \mathbf{F} \quad (10)$$

where  $\mathbf{K}$  is the stiffness matrix,  $\mathbf{U}$  is the displacement field and  $\mathbf{F}$  is the mechanical load vector. As Eq. (10) represents the global system of all finite elements,  $\mathbf{K}$  is assembled from the element stiffness matrices as  $\mathbf{K} = \sum_e^{N_e} \mathbf{K}^e$ .

The element stiffness matrix  $\mathbf{K}^e$ , as expressed in Eq. (11) for 2D problems considering square elements, directly follows from the derivation of the FEM equation.

$$\mathbf{K}^e = \int_{\Omega_e} \mathbf{B}^T \mathbf{D} \mathbf{B} d\Omega = \iint_{\Omega_e} \mathbf{B}^T \mathbf{D} \mathbf{B} t dx dy \quad (11)$$

where  $\mathbf{B}$  is the strain-displacement matrix.

### 2.1.3 Thermo-mechanical load vector

The thermal and mechanical responses of the structure are weakly coupled and this thermo-mechanical coupling is governed by thermal expansion. Apart from the mechanical contribution  $\mathbf{F}_m$ , the global load vector  $\mathbf{F}$  is updated with thermally induced nodal forces in Eq. (12), which are assembled in the thermo-mechanical load vector  $\mathbf{F}_{th}$ .

$$\mathbf{F} = \mathbf{F}_m + \mathbf{F}_{th} \quad (12)$$

The definition of the thermo-mechanical load vector is derived from the FEM equation (Zienkiewicz et al., 2013) and the element thermo-mechanical load vector  $\mathbf{F}_{th}^e$  is given by Eq. (13) (Logan, 2016).

$$\mathbf{F}_{th}^e = \int_{\Omega_e} \mathbf{B}^T \mathbf{D} \boldsymbol{\varepsilon}_{th} d\Omega = \iint_{\Omega_e} \mathbf{B}^T \mathbf{D} \boldsymbol{\varepsilon}_{th} t dx dy \quad (13)$$

where  $\boldsymbol{\varepsilon}_{th}$  is the thermal strain tensor given by Eq. (14) in Voigt notation considering 2D plane stress and an isotropic material.

$$\boldsymbol{\varepsilon}_{th} = \begin{bmatrix} \alpha \Delta T \\ \alpha \Delta T \\ 0 \end{bmatrix} \quad (14)$$

where  $\alpha$  represents the coefficient of thermal expansion. The temperature difference  $\Delta T$  is calculated in Eq. (15) as the difference between the computed element temperature  $T_e$  and the reference temperature  $T_{ref}$ .

$$\Delta T = T_e - T_{ref} = \frac{1}{4} \sum_{i=1}^4 T_i - T_{ref} \quad (15)$$

where the element temperature  $T_e$  is calculated as the arithmetic average of the nodal temperatures in the corners of the element  $T_i$  for  $i = 1, \dots, 4$  (cf. Figure 2).

In case multiple elements are connected by the same nodes, the equivalent nodal forces associated with each mechanical degree of freedom (DoF) need to be assembled (or cumulated) into the global thermo-mechanical load vector  $\mathbf{F}_{th}$  in Eq. (16) (see Section 2.2.2 and 3.2).

$$\mathbf{F}_{th} = \sum_e^{N_e} \mathbf{F}_{th}^e \quad (16)$$

## 2.2 Topology optimization formulation

### 2.2.1 Optimization problem

The optimization problem considered in this paper is expressed in Eq. (17). The problem involves the minimization of structural compliance  $c$  subjected to a volume constraint  $V$  and governed by a weakly coupled thermo-mechanical analysis considering SHC as described in Section 2.1. The design variables  $\mathbf{x}$  are the relative element densities for the optimization of a two-phase material layout with a value between 0 (void) and 1 (solid) (Bendsøe & Sigmund, 2003).

$$\begin{aligned} \text{Find } & \mathbf{x} = (x_1, x_2, \dots, x_{N_e}) \\ \min_{\mathbf{x}} & c = \mathbf{F}^T \mathbf{U} \\ \text{s. t. } & V = V(\mathbf{x}) - \varphi V_0 \leq 0 \\ & \mathbf{K}_{th} \mathbf{T} = \mathbf{Q} \\ & \mathbf{K} \mathbf{U} = \mathbf{F}_m + \mathbf{F}_{th} \\ & 0 \leq x_e \leq 1 \text{ with } x_e \in \mathbf{x} \end{aligned} \quad (17)$$

where  $V(\mathbf{x})$  is the volume for a design  $\mathbf{x}$ ,  $\varphi$  is the prescribed volume fraction and  $V_0 = N_e V_e$  is the total volume of a solid design where  $V_e = z^2 t$  is the solid element volume and  $z$  is the element edge length.

The volume  $V(\mathbf{x})$  is expressed in Eq. (18) as the sum of the element densities multiplied with the solid element volume.

$$V(\mathbf{x}) = \sum_{i=1}^{N_e} x_i V_e \quad (18)$$

The expression for the elastic compliance  $c$  can be reformulated in terms of the displacement field  $\mathbf{U}$  and stiffness matrix  $\mathbf{K}$  by substituting the mechanical state equation. Since  $\mathbf{K}$  is symmetric, and thus  $\mathbf{F}^T = \mathbf{U}^T \mathbf{K}$ , then the expression for the compliance is elaborated in Eq. (19).

$$c = \mathbf{U}^T \mathbf{K} \mathbf{U} = \sum_e^{N_e} \mathbf{U}_e^T \mathbf{K}^e \mathbf{U}_e = \sum_e^{N_e} E(x_e) \mathbf{U}_e^T \mathbf{K}^0 \mathbf{U}_e \quad (19)$$

where  $\mathbf{U}_e$  is the element displacement vector and  $E(x_e)$  is the density function for the stiffness as discussed in the next section.

In the developed TO procedure, a density filter is used in order to avoid the issue of checkerboarding (Bendsøe & Sigmund, 2003). The implementation and the modification of the sensitivities (see Section 2.2.3) are directly adopted from (Andreassen et al., 2011). Furthermore, the method of moving asymptotes (MMA) (Svanberg, 1987) is used as the gradient-based optimizer for updating the design variables, as it allows for more flexibility for further extensions of the implementation using multiple constraints.

## 2.2.2 Material interpolation

With regard to the density-based TO approach, the material properties are expressed in function of the relative element densities, i.e. the design variables  $\mathbf{x}$  in the optimization problem. A modification of the SIMP method based on (Sigmund, 2007) is employed for the interpolation of the material properties, for which a lower bound value is added in order to avoid singularities in the coefficient matrices of the governing state equations. The constant material properties from Section 2.1 are replaced by their corresponding density functions from now on.

The density function for the Young's modulus  $E(\mathbf{x})$  and its first derivative with respect to the design variables  $\mathbf{x}$  are given by Eq. (20).

$$\begin{aligned} E(\mathbf{x}) &= E_{min} + \mathbf{x}^{p_E} \Delta E \\ \frac{\partial E(\mathbf{x})}{\partial \mathbf{x}} &= p_E \mathbf{x}^{p_E-1} \Delta E \end{aligned} \quad (20)$$

where  $p_E$  is the penalization factor (with typically  $p_E \geq 1$  (Stolpe & Svanberg, 2001)),  $\mathbf{x}$  the vector of design variables and  $\Delta E = E_0 - E_{min}$  in which  $E_0$  is the Young's modulus for a solid element ( $x_e = 1$ ) and  $E_{min}$  is the lower bound value (usually taken as  $10^{-9}E_0$ ) for the void material phase. Note that  $\partial E(x_j)/\partial x_i = 0$  when  $i \neq j$ ,  $\forall i, j = 1, \dots, N_e$ .

The thermal conductivity  $\kappa(\mathbf{x})$  is penalized in a similar manner as the modulus of elasticity. The corresponding density function and its first derivative are provided in Eq. (21).

$$\begin{aligned} \kappa(\mathbf{x}) &= \kappa_{min} + \mathbf{x}^{p_\kappa} \Delta \kappa \\ \frac{\partial \kappa(\mathbf{x})}{\partial \mathbf{x}} &= p_\kappa \mathbf{x}^{p_\kappa-1} \Delta \kappa \end{aligned} \quad (21)$$

where  $p_\kappa$  is the penalization factor and  $\Delta \kappa = \kappa_0 - \kappa_{min}$  in which  $\kappa_0$  is the thermal conductivity for a solid element and  $\kappa_{min}$  is the lower bound value. Note that  $\partial \kappa(x_j)/\partial x_i = 0$  when  $i \neq j$ ,  $\forall i, j = 1, \dots, N_e$ .

Furthermore, the coefficient matrices  $\mathbf{K}_{th}$  and  $\mathbf{K}$  for the thermal and mechanical state equations can be reformulated in Eq. (22) by substituting the constant material properties by their respective density functions from Eq. (20) and Eq. (21).

$$\begin{aligned} \mathbf{K}_{th} &= \sum_e^{N_e} \kappa(x_e) \mathbf{K}_{th}^0 \\ \mathbf{K} &= \sum_e^{N_e} E(x_e) \mathbf{K}^0 \end{aligned} \quad (22)$$

where  $\mathbf{K}_{th}^0$  and  $\mathbf{K}^0$  are the constant element (thermal) stiffness matrices, independent of the design variables  $\mathbf{x}$ .

Apart from the coefficient matrices, the material properties  $E(\mathbf{x})$  and  $\alpha(\mathbf{x})$  also appear in the definition of the thermo-mechanical load vector in Eq. (13). As both properties can be considered density-dependent, they are combined into a single thermal stress coefficient (TSC), denoted  $\beta(\mathbf{x})$  in Eq. (23). This parameter was introduced by Gao and Zhang (2010), assuming the same Poisson ratio for each material phase (Gao et al., 2016).

$$\beta(\mathbf{x}) = E(\mathbf{x})\alpha(\mathbf{x}) = E_0\alpha f_\beta(\mathbf{x}) \quad (23)$$

where  $f_\beta(\mathbf{x})$  is the coefficient that is dependent on the design variables  $\mathbf{x}$ .

The TSC is penalized similar to  $E$  and  $\kappa$ , using a separate penalization factor  $p_\beta$ . For example, the coefficient  $f_\beta(\mathbf{x})$  is expressed for the SIMP method in Eq. (24).

$$f_\beta(\mathbf{x}) = \frac{E_{min}}{E_0} + \mathbf{x}^{p_\beta} \left(1 - \frac{E_{min}}{E_0}\right) \quad (24)$$

As a result, the element thermo-mechanical load vector  $\mathbf{F}_{th}^e$  is rewritten to include the TSC in Eq. (25) as a  $1 \times 8$  vector, as it will be used further in the sensitivity analysis (see Section 2.2.3).

$$\mathbf{F}_{th}^e = [f_{th,1} \quad \dots \quad f_{th,8}] = \frac{\beta(x_e)\Delta T z t}{2(1-\nu)} \mathbf{I}_{tm}^e \quad (25)$$

where  $f_{th,i}$  represents the nodal forces for each mechanical DoF (with  $i = 1, \dots, 8$ ) in element  $e$  according to Figure 2 and  $\mathbf{I}_{tm}^e = [-1 \quad -1 \quad 1 \quad -1 \quad 1 \quad 1 \quad -1 \quad 1]$ .

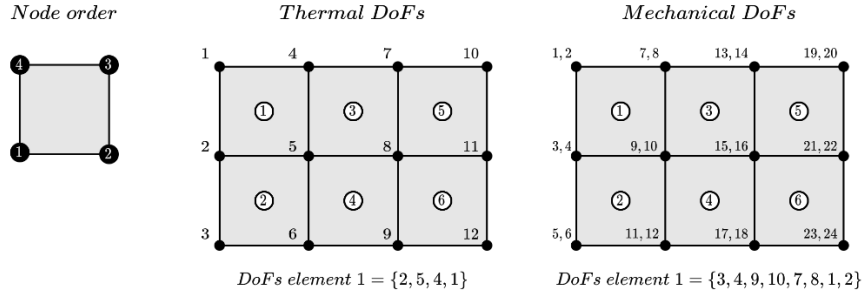


Figure 2: Node order, thermal and mechanical DoFs

The temperature difference  $\Delta T$  in Eq. (25) is implicitly dependent on the relative element density  $x_e$  in case the thermal finite element analysis (FEA) is required to calculate a non-uniform temperature field  $\mathbf{T}(\mathbf{x})$ , as  $T_e \equiv T_e(\mathbf{T}(\mathbf{x}))$ . This is straightforward, as the temperature field  $\mathbf{T}$  is dependent on the material distribution and the associated thermal properties of the elements.

By further analyzing Eq. (25), the equivalent nodal forces due to thermal expansion (corresponding to the node numbering in Figure 2) are dependent on the dimensions of the elements, apart from the (thermo-)mechanical properties. As a result, depending on the sign of the temperature difference  $\Delta T$ , an element would either contract or expand, assuming  $\alpha > 0$  for typical construction materials (see Figure 3).

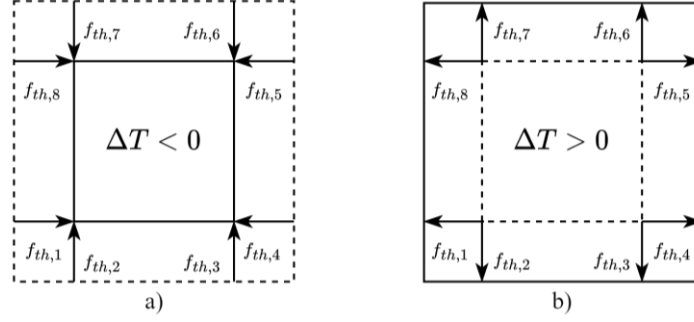


Figure 3: Equivalent nodal forces for thermal expansion: a) contraction and b) expansion

### 2.2.3 Sensitivity analysis

In order to use a gradient optimizer such as the MMA algorithm employed in this paper, the sensitivities for the compliance objective and volume constraint with respect to the design variables need to be determined.

The sensitivity analysis for the volume constraint  $V$  is straightforward. The derivative with respect to the  $\mathbf{x}$  is calculated in Eq. (26) based on Eqs. (17) and (18).

$$\frac{dV}{d\mathbf{x}} = \frac{dV(\mathbf{x})}{d\mathbf{x}} = \frac{d}{d\mathbf{x}} \left( \sum_{i=1}^{N_e} x_i V_e \right) = V_e \quad (26)$$

The sensitivity analysis for the compliance objective is more complicated due to the design-dependency and temperature-dependency of the thermo-mechanical load vector. Hence, the nested formulation of the objective function  $c$  is given by Eq. (27).

$$c(\mathbf{x}, \mathbf{T}(\mathbf{x}), \mathbf{U}(\mathbf{x})) = \mathbf{F}^T(\mathbf{x}, \mathbf{T}(\mathbf{x})) \mathbf{U}(\mathbf{x}) \quad (27)$$

where the compliance  $c$  is dependent on the design variables  $\mathbf{x}$  and the state variables  $\mathbf{U}(\mathbf{x})$  and  $\mathbf{T}(\mathbf{x})$  from the mechanical and thermal state equations in Eq. (17) respectively.

In this paper, the analytical adjoint method is employed to carry out the sensitivity analysis (Allaire, 2015; Tortorelli & Michaleris, 1994; Zheng et al., 2009). In order to obtain the corresponding sensitivities in a computationally efficient manner, an adjoint system is solved instead of calculating the implicit derivatives of the state variables  $\mathbf{T}$  and  $\mathbf{U}$  directly with respect to the design variables. Therefore, an augmented objective function  $\hat{c}$  is first constructed in Eq. (28).

$$\hat{c} = c + \boldsymbol{\lambda}^T(\mathbf{R}_m) + \boldsymbol{\mu}^T(\mathbf{R}_{th}) \quad (28)$$

where  $\boldsymbol{\lambda}$  and  $\boldsymbol{\mu}$  are Lagrange multipliers or adjoint variables and  $\mathbf{R}_{th}$  and  $\mathbf{R}_m$  are the residuals for the thermal and mechanical state equations respectively, as expressed in Eq. (29). Note that under the equality constraints in Eq. (17), governed by the thermal and mechanical state equations, the residuals are both equal to zero, henceforth  $\hat{c} \equiv c$ .

$$\begin{aligned} \mathbf{R}_{th} &\equiv \mathbf{K}_{th}(\mathbf{x})\mathbf{T}(\mathbf{x}) - \mathbf{Q}(\mathbf{x}) = 0 \\ \mathbf{R}_m &\equiv \mathbf{K}(\mathbf{x})\mathbf{U}(\mathbf{x}) - \mathbf{F}(\mathbf{x}, \mathbf{T}(\mathbf{x})) = 0 \end{aligned} \quad (29)$$

According to Eq. (12),  $\mathbf{F}$  is comprised of the mechanical and thermo-mechanical load vector,  $\mathbf{F}_m$  and  $\mathbf{F}_{th}$  respectively, of which the former is not dependent on the design or state variables. The nested formulation for  $\mathbf{F}$  is expressed in Eq. (30).

$$\mathbf{F}(\mathbf{x}, \mathbf{T}(\mathbf{x})) = \mathbf{F}_m + \mathbf{F}_{th}(\mathbf{x}, \mathbf{T}(\mathbf{x})) \quad (30)$$

The vectors and matrices will further be written in an implicit form without explicitly mentioning the dependencies of the design and state variables.

The total derivative of augmented objective function  $\hat{c}$  with respect to  $\mathbf{x}$  is determined in Eq. (31).

$$\frac{d\hat{c}}{d\mathbf{x}} = \frac{dc}{d\mathbf{x}} + \frac{d\lambda^T}{d\mathbf{x}} \mathbf{R}_m + \lambda^T \frac{d\mathbf{R}_m}{d\mathbf{x}} + \frac{d\boldsymbol{\mu}^T}{d\mathbf{x}} \mathbf{R}_{th} + \boldsymbol{\mu}^T \frac{d\mathbf{R}_{th}}{d\mathbf{x}} = \frac{dc}{d\mathbf{x}} + \lambda^T \frac{d\mathbf{R}_m}{d\mathbf{x}} + \boldsymbol{\mu}^T \frac{d\mathbf{R}_{th}}{d\mathbf{x}} \quad (31)$$

where the terms containing the residuals are eliminated due to Eq. (29).

The total derivatives of the three terms in Eq. (31) are determined in Eq. (32) by applying the chain rule for multivariable differentiation with respect to the design and state variables  $\mathbf{x}$ ,  $\mathbf{U}$  and  $\mathbf{T}$ .

$$\left\{ \begin{array}{l} \frac{dc}{d\mathbf{x}} = \frac{\partial c}{\partial \mathbf{x}} + \frac{\partial c}{\partial \mathbf{U}} \frac{d\mathbf{U}}{d\mathbf{x}} + \frac{\partial c}{\partial \mathbf{T}} \frac{d\mathbf{T}}{d\mathbf{x}} = \left( \frac{\partial \mathbf{F}^T}{\partial \mathbf{x}} \mathbf{U} \right) + \mathbf{F}^T \frac{d\mathbf{U}}{d\mathbf{x}} + \frac{\partial \mathbf{F}^T}{\partial \mathbf{T}} \mathbf{U} \frac{d\mathbf{T}}{d\mathbf{x}} \\ \frac{d\mathbf{R}_m}{d\mathbf{x}} = \frac{\partial \mathbf{R}_m}{\partial \mathbf{x}} + \frac{\partial \mathbf{R}_m}{\partial \mathbf{U}} \frac{d\mathbf{U}}{d\mathbf{x}} + \frac{\partial \mathbf{R}_m}{\partial \mathbf{T}} \frac{d\mathbf{T}}{d\mathbf{x}} = \left( \frac{\partial \mathbf{K}}{\partial \mathbf{x}} \mathbf{U} - \frac{\partial \mathbf{F}}{\partial \mathbf{x}} \right) + \mathbf{K} \frac{d\mathbf{U}}{d\mathbf{x}} - \frac{\partial \mathbf{F}}{\partial \mathbf{T}} \frac{d\mathbf{T}}{d\mathbf{x}} \\ \frac{d\mathbf{R}_{th}}{d\mathbf{x}} = \frac{\partial \mathbf{R}_{th}}{\partial \mathbf{x}} + \frac{\partial \mathbf{R}_{th}}{\partial \mathbf{T}} \frac{d\mathbf{T}}{d\mathbf{x}} = \left( \frac{\partial \mathbf{K}_{th}}{\partial \mathbf{x}} \mathbf{T} - \frac{\partial \mathbf{Q}}{\partial \mathbf{x}} \right) + \mathbf{K}_{th} \frac{d\mathbf{T}}{d\mathbf{x}} \end{array} \right. \quad (32)$$

The derivatives determined in Eq. (32) are substituted into Eq. (31) and further rearranged and expressed in terms of explicit derivatives (in square brackets) and the implicit derivatives of the state variables  $d\mathbf{U}/d\mathbf{x}$  and  $d\mathbf{T}/d\mathbf{x}$  in Eq. (33).

$$\begin{aligned} \frac{d\hat{c}}{d\mathbf{x}} = & \left[ \frac{\partial \mathbf{F}^T}{\partial \mathbf{x}} \mathbf{U} + \lambda^T \frac{\partial \mathbf{K}}{\partial \mathbf{x}} \mathbf{U} - \lambda^T \frac{\partial \mathbf{F}}{\partial \mathbf{x}} + \boldsymbol{\mu}^T \frac{\partial \mathbf{K}_{th}}{\partial \mathbf{x}} \mathbf{T} - \boldsymbol{\mu} \frac{\partial \mathbf{Q}}{\partial \mathbf{x}} \right] + (\mathbf{F}^T + \lambda^T \mathbf{K}) \frac{d\mathbf{U}}{d\mathbf{x}} \\ & + \left( \frac{\partial \mathbf{F}^T}{\partial \mathbf{T}} \mathbf{U} - \lambda^T \frac{\partial \mathbf{F}}{\partial \mathbf{T}} + \boldsymbol{\mu}^T \mathbf{K}_{th} \right) \frac{d\mathbf{T}}{d\mathbf{x}} \end{aligned} \quad (33)$$

In order to avoid the computationally expensive calculation of the implicit derivatives, the corresponding terms can be eliminated in case the adjoint variables are solutions to the adjoint systems defined in Eq. (34).

$$\left\{ \begin{array}{l} \mathbf{F}^T + \lambda^T \mathbf{K} = 0 \\ \frac{\partial \mathbf{F}^T}{\partial \mathbf{T}} \mathbf{U} - \lambda^T \frac{\partial \mathbf{F}}{\partial \mathbf{T}} + \boldsymbol{\mu}^T \mathbf{K}_{th} = 0 \end{array} \right. \quad (34)$$

The solutions to the adjoint systems are provided in Eq. (35). Note that the first adjoint system of equations is self-adjoint as  $\boldsymbol{\lambda} = -\mathbf{U}$ , which is already obtained by the mechanical FEA.

$$\left\{ \begin{array}{l} \boldsymbol{\lambda} = -\mathbf{K}^{-1} \mathbf{F} = -\mathbf{U} \\ \boldsymbol{\mu} = \mathbf{K}_{th}^{-1} \left( -2\mathbf{U}^T \frac{\partial \mathbf{F}}{\partial \mathbf{T}} \right) = \mathbf{K}_{th}^{-1} \mathbf{Q}_{adj} \end{array} \right. \quad (35)$$

where  $\mathbf{Q}_{adj}$  represents a fictitious heat load vector for the adjoint problem.

By eliminating the implicit terms in Eq. (33), the final expression for the sensitivities is obtained in Eq. (36). Further derivation with respect to the filtered densities (due to the density filtering) is adapted from (Andreassen et al., 2011).

$$\frac{dc}{d\mathbf{x}} \equiv \frac{d\hat{c}}{d\mathbf{x}} = \frac{\partial \mathbf{F}^T}{\partial \mathbf{x}} \mathbf{U} + \boldsymbol{\lambda}^T \left( \frac{\partial \mathbf{K}}{\partial \mathbf{x}} \mathbf{U} - \frac{\partial \mathbf{F}}{\partial \mathbf{x}} \right) + \boldsymbol{\mu}^T \left( \frac{\partial \mathbf{K}_{th}}{\partial \mathbf{x}} \mathbf{T} - \frac{\partial \mathbf{Q}}{\partial \mathbf{x}} \right) \quad (36)$$

This is further simplified to Eq. (37) (independently reported by Van Den Hende & Van Paeppegem (2021)) by substituting the adjoint variable  $\boldsymbol{\lambda}$  from Eq. (35). Herein, it is assumed that  $\partial \mathbf{Q} / \partial \mathbf{x} = 0$  since the heat loads are considered to be independent of  $\mathbf{x}$ .

$$\frac{dc}{d\mathbf{x}} = -\mathbf{U}^T \frac{\partial \mathbf{K}}{\partial \mathbf{x}} \mathbf{U} + 2\mathbf{U}^T \frac{\partial \mathbf{F}}{\partial \mathbf{x}} + \boldsymbol{\mu}^T \frac{\partial \mathbf{K}_{th}}{\partial \mathbf{x}} \mathbf{T} \quad (37)$$

where adjoint variable  $\boldsymbol{\mu}$  is calculated separately according to Eq. (35).

As such one additional FEA needs to be carried out to calculate the sensitivities. This results in a total of three linear systems to be solved per iteration for a TO procedure considering thermo-mechanical loading due to SHC.

The first term in Eq. (37) contains the derivative of the stiffness matrix  $\mathbf{K}$ , which is calculated in Eq. (38), as only the Young's modulus is a function of  $x_e$ .

$$\frac{\partial \mathbf{K}}{\partial \mathbf{x}} = \sum_e^{N_e} \frac{\partial \mathbf{K}^e}{\partial x_e} = \sum_e^{N_e} \left( \frac{\partial E(x_e)}{\partial x_e} \mathbf{K}^0 \right) \quad (38)$$

where  $\partial E(x_e) / \partial x_e$  is calculated according to Eq. (20).

Similarly, the derivative of the thermal stiffness matrix  $\mathbf{K}_{th}$  is provided in Eq. (39) for the third term in Eq. (37).

$$\frac{\partial \mathbf{K}_{th}}{\partial \mathbf{x}} = \sum_e^{N_e} \frac{\partial \mathbf{K}_{th}^e}{\partial x_e} = \sum_e^{N_e} \left( \frac{\partial \kappa(x_e)}{\partial x_e} \mathbf{K}_{th}^0 \right) \quad (39)$$

where  $\partial \kappa(x_e) / \partial x_e$  is calculated according to Eq. (21).

Furthermore, the derivative of the global load vector  $\mathbf{F}$  with respect to  $\mathbf{x}$  is expressed in Eq. (40), as it appears in the second term of Eq. (37).

$$\frac{\partial \mathbf{F}}{\partial \mathbf{x}} = \frac{\partial \left( \mathbf{F}_m + \mathbf{F}_{th}(\mathbf{x}, \mathbf{T}(\mathbf{x})) \right)}{\partial \mathbf{x}} = \frac{\partial \mathbf{F}_{th}}{\partial \mathbf{x}} \neq 0 \quad (40)$$

The mechanical load vector  $\mathbf{F}_m$  containing the externally applied forces is fixed and not dependent on the design variables, such that its derivative with respect to  $\mathbf{x}$  is zero. However, the thermo-mechanical load vector  $\mathbf{F}_{th}$  is design-dependent, both explicitly and implicitly in terms of  $\beta(\mathbf{x})$  and  $\mathbf{T}(\mathbf{x})$  respectively. Moreover, if the element densities change during the optimization, the corresponding temperature field will be influenced accordingly. As a result, the derivative of the thermo-mechanical load vector is assumed to be nonzero.

Subsequently, the derivation of the thermo-mechanical load vector  $\mathbf{F}_{th}$  with respect to  $\mathbf{x}$  is carried out in Eq. (41), taking into account Eq. (25).

$$\frac{\partial \mathbf{F}_{th}}{\partial \mathbf{x}} = \frac{\partial}{\partial \mathbf{x}} \left( \sum_e^{N_e} \mathbf{F}_{th}^e \right) = \sum_e^{N_e} \left( \frac{\partial \beta(\mathbf{x})}{\partial \mathbf{x}} \frac{\Delta T(\mathbf{T}) z t}{2(1-\nu)} \mathbf{I}_{tm}^e \right) \quad (41)$$

The derivative of the TSC, i.e.  $\partial \beta(\mathbf{x}) / \partial \mathbf{x}$ , is easily determined from its definition in Eq. (23). Note that Eq. (41) determines the partial derivative with respect to  $\mathbf{x}$  and only  $\beta(\mathbf{x})$  is an explicit function of  $\mathbf{x}$ .

Finally, in order to calculate the adjoint variable  $\boldsymbol{\mu}$ , the derivative of  $\mathbf{F}$  with respect to the temperature field  $\mathbf{T}$  needs to be determined. In essence, the matrix  $\partial \mathbf{F} / \partial \mathbf{T}$  contains the derivatives of each nodal force (i.e. for each mechanical DoF) with respect to each nodal temperature in  $\mathbf{T}$ , as expressed in Eq. (42), assuming only the thermo-mechanical contribution  $\mathbf{F}_{th}$  is dependent on the nodal temperatures. In order to efficiently determine  $\partial \mathbf{F} / \partial \mathbf{T}$ , the thermo-mechanical load vector  $\mathbf{F}_{th}$  is reformulated in terms of the nodal temperatures (see Section 3.3).

$$\frac{\partial \mathbf{F}}{\partial \mathbf{T}} = \frac{\partial \mathbf{F}_{th}}{\partial \mathbf{T}} = \frac{\partial (F_{th}^1, \dots, F_{th}^{2N})}{\partial (T^1, \dots, T^N)} \quad (42)$$

where  $N$  and  $2N$  are the numbers of DoFs for the thermal and mechanical governing problems, e.g. 12 and 24 in Figure 2, respectively.

### 3 MATLAB implementation

The proposed TO procedure involving thermo-mechanical loading is developed in MATLAB. In this section some insights are provided regarding its implementation based on the popular, educational 88-line MATLAB code by Andreassen et al. (2011). Many of the programming aspects are specifically tailored to the format of this code. However, the way the matrices are transformed into proper code is useful for any platform or programming language. The focus of this section is mainly on the additional lines of code required to extend the existing 88-line code to include thermo-mechanical loading. The developed MATLAB code is written concisely into 138 lines, and it is made available in Appendix 2 with references to specific line numbers in the following subsections.

Note that the code is developed with a notion of dimensionality in view of modelling full-scale structures subjected to realistic (thermal) loads. The input values for the material properties and the dimensions implicitly assume the use of SI(mm) units. In addition, the thickness parameter  $t$  is included in the coefficient matrices and the thermo-mechanical load vector as it influences the optimization in case of thermo-mechanical loading (see Section 4.3.3).

#### 3.1 Thermal analysis

The implementation of the thermal FEA is an adaptation on the code provided by Vantighem et al. (2019), where the thermal FEA was employed without thermo-mechanical coupling. An extra set of material parameters is introduced for the thermal conductivity in line 10. In lines 14-22 the preparation of the thermal FEA is carried out, providing the necessary arrays of indices and pre-allocation of vectors and matrices for the assembly of the thermal stiffness matrix. In this study, bilinear square heat transfer elements with 4 nodes and 1 DoF per node (i.e. nodal temperature) are used. In lines 24-32 the boundary conditions and node sets are initialized, and the heat load vector is pre-allocated. Furthermore, in lines 86-87 the thermal conductivity and its derivative are expressed as density functions and in lines 91-92 the thermal stiffness matrix is assembled.

The implementation of the thermal FEA is analogous to that of the static mechanical analysis in the original 88-line MATLAB code (Andreassen et al., 2011). However, depending on the type of boundary conditions, the linear system is solved differently. In the presented case study (see Section 4) Dirichlet conditions are used for the thermal loading. Therefore, the expression for the thermal FEA from Eq. (3) is explicitly written (and rearranged) in terms of the known (constrained) and unknown (free) DoFs, given by Eq. (43).

$$\begin{bmatrix} \mathbf{K}_{th}^{cc} & \mathbf{K}_{th}^{cf} \\ \mathbf{K}_{th}^{fc} & \mathbf{K}_{th}^{ff} \end{bmatrix} \begin{bmatrix} \mathbf{T}^c \\ \mathbf{T}^f \end{bmatrix} = \begin{bmatrix} \mathbf{Q}^c \\ \mathbf{Q}^f \end{bmatrix} \quad (43)$$

where superscripts  $c$  and  $f$  represent the indices of the constrained and free DoFs respectively. Double superscripts refer to the corresponding rows and columns respectively.

From Eq. (43), the expression for the unknown temperatures  $\mathbf{T}^f$  is expressed in Eq. (44).

$$\mathbf{T}^f = \mathbf{K}_{th}^{ff-1} (\mathbf{Q}^f - \mathbf{K}_{th}^{fc} \mathbf{T}^c) \quad (44)$$

which is expressed in line 93 using the  $\backslash$ -operator for efficient use of Cholesky decomposition when considering symmetric matrices.

## 3.2 Thermo-mechanical load vector

In order to efficiently calculate the global thermo-mechanical load vector  $\mathbf{F}_{th}$ , two new variables  $\mathbf{T}_T$  and  $\mathbf{T}_{TM}$  are introduced, which represent the element-temperature matrix and thermo-mechanical transformation matrix respectively. The global thermo-mechanical load vector can then be expressed as a matrix multiplication in Eq. (45) (line 96).

$$\mathbf{F}_{th} = \mathbf{T}_{TM}^T (\widehat{\mathbf{F}}_{th}^e \odot \Delta \mathbf{T}) \quad (45)$$

where  $\widehat{\mathbf{F}}_{th}^e$  is expressed in Eq. (46),  $\odot$  is the element-wise multiplication operator and  $\Delta \mathbf{T}$  is the elemental temperature difference vector expressed in Eq. (47) (line 95).

$$\widehat{\mathbf{F}}_{th}^e = \frac{\beta(\mathbf{x})tz}{2(1-\nu)} \quad (46)$$

The  $N_e \times N$  matrix  $\mathbf{T}_T$  (line 51) transforms the global (nodal) temperature difference vector  $(\mathbf{T} - \mathbf{T}_{ref})$  into the elemental temperature vector by left multiplication, which results in the arithmetic average temperature per element. Each row of  $\mathbf{T}_T$  contains the nodal temperature contributions to the corresponding element temperature, or in other words, each rows consists of zeros except for the 4 thermal DoFs associated with the element nodes, which have a value of 1/4.

$$\Delta \mathbf{T} = \mathbf{T}_T (\mathbf{T} - \mathbf{T}_{ref}) \quad (47)$$

Similarly, the  $N_e \times 2N$  thermo-mechanical transformation matrix  $\mathbf{T}_{TM}$  (line 52) transforms the elemental contributions to the thermo-mechanical loading due to thermal expansion into an equivalent nodal force vector. Each row of  $\mathbf{T}_{TM}$  contains the elemental contribution to the corresponding nodal forces, or in other words, each rows consists of zeros except for the 8 mechanical DoFs associated with the element nodes, which have a value of (-)1, depending on the relative position of the DoF to the element centroid (see Figure 3). The sign of the nodal forces is already captured by the vector  $\mathbf{I}_{tm}^e$  (line 50), as discussed in Section 2.2.2. As a result,  $\mathbf{F}_{th}$  contains the corresponding (nodal) force for each mechanical DoF, in which all contributions of neighboring elements are included in the magnitude and direction of the forces.

### 3.3 Sensitivity analysis

Although the volume  $V(\mathbf{x})$  and its derivative are expressed in Eq. (18) and Eq. (26) considering the element edge length  $z$  and thickness  $t$ , the implementation in MATLAB is based on a unit element and thickness. This simplification is allowed as the volume constraint can be scaled by  $V_0$  without altering the result, which is preferred in combination with MMA. Therefore, the volume and its derivative are reformulated in Eq. (48) and likewise implemented in lines 103-104.

$$V(\mathbf{x}) = \frac{1}{N_e} \sum_{i=1}^{N_e} x_i \quad (48)$$

$$\frac{dV}{d\mathbf{x}} = \frac{1}{N_e}$$

In Section 2.2.3, the analytical expression for the sensitivity of the compliance objective with respect to the design variables is derived. The first term of Eq. (37) is identical to the sensitivity of the compliance in case only mechanical loading is considered and its implementation in MATLAB (lines 105-107) is similar to (Andreassen et al., 2011).

For the second term of Eq. (37), the displacement field  $\mathbf{U}$  is rearranged, such that each row contains the DoFs corresponding with each element, and subsequently right multiplied with the vector  $\mathbf{I}_{tm}^e$ . Then the matrices are multiplied element-wise to obtain the second contribution to the sensitivities for each design variable (line 108). An abstraction of the expression is provided in Eq. (49).

$$2\mathbf{U}^T \frac{\partial \mathbf{F}}{\partial \mathbf{x}} = \sum_e^{N_e} 2\mathbf{U}_e^T \frac{\partial \mathbf{F}^e}{\partial \mathbf{x}} = \sum_e^{N_e} 2 \frac{E_0 \alpha t z}{2(1-\nu)} (\mathbf{U}_e^T \mathbf{I}_{tm}^e)^T \odot \frac{\partial f_\beta(x_e)}{\partial x_e} \odot \Delta T \quad (49)$$

The third term of Eq. (37) contains the adjoint variable  $\boldsymbol{\mu}$  for which the calculation of  $\partial \mathbf{F} / \partial \mathbf{T}$  is required. This  $2N \times N$  matrix is easily expressed by employing the transformation matrices  $\mathbf{T}_T$  and  $\mathbf{T}_{TM}$  in Eq. (50). Note that the order of operations depends on the dimensions of the resulting matrices and in turn influences the efficiency of the calculation.

$$\frac{\partial \mathbf{F}}{\partial \mathbf{T}} = (\mathbf{T}_{TM}^T \odot \widehat{\mathbf{F}}_{th}^e)^T \mathbf{T}_T \quad (50)$$

where implicitly substituted  $\partial(\Delta T) / \partial \mathbf{T} = \mathbf{T}_T$  based on Eq. (47), as only the temperature difference vector is dependent on  $\mathbf{T}$  in Eq. (25).

The fictitious heat load vector  $\mathbf{Q}_{adj}$  from Eq. (35) is calculated in line 109 and the adjoint variable  $\boldsymbol{\mu}$  is determined in line 110. Subsequently, the third term in the sensitivities (line 111) is determined in a similar manner as the first term.

In line 112 all three contributions are cumulated to obtain the compliance sensitivities. The compliance objective and the corresponding sensitivities are rescaled in lines 114-115 for the use of MMA (lines 120-129) as discussed in the next section.

## 4 Numerical example

In this section a numerical example is provided in order to demonstrate the proposed procedure for thermo-elastic TO considering steady-state heat conduction. Subsequently, the effect of the sensitivity analysis, thermo-mechanical load ratio, the volume constraint and material interpolation on the optimized solution are investigated.

### 4.1 Problem formulation

A simply supported Messerschmitt-Bölkow-Blohm (MBB) beam is subjected to a downwards point load  $F_m$  in the middle of the top edge and a set of fixed thermal Dirichlet conditions, as illustrated in Figure 4. The top edge is fixed at an ambient temperature  $T_a = 0^\circ\text{C}$  and the bottom edge is exposed to an elevated temperature  $T_f = 800^\circ\text{C}$  by default, imposing a large thermal gradient. The fixed temperatures are imposed on the corresponding thermal DoFs that coincide with both edges. The total mechanical load  $F_m$  is equal to  $10\text{ kN}$ . Here, the MBB beam is modelled symmetrically to save on computation time, so only half of the total mechanical load is applied. The half beam structure has a length  $L = 1200\text{ mm}$ , a height  $h = 400\text{ mm}$ , a thickness  $t = 10\text{ mm}$  and the design domain is discretized into a mesh of  $120 \times 40$  square elements with an edge length of  $z = 10\text{ mm}$  by default. The dimensions, loads and BCs are fixed to the default values in all optimizations unless specified otherwise.

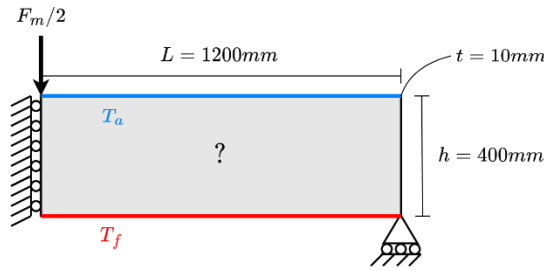


Figure 4: MBB beam model

The two-phase material resembles concrete in the solid phase ( $x_e = 1$ ) and a fictitious, mechanically weak, thermally insulating material (e.g. mineral wool) in the void phase ( $x_e = 0$ ). The material properties for both phases are listed in Table 1, where the Poisson's ratio and coefficient of thermal expansion are assumed constant.

Table 1: Material properties concrete – insulation

$E - E_{min}$ [MPa]	$\nu$ [-]	$\alpha$ [1/K]	$\kappa - \kappa_{min}$ [W/mK]
30e3 – 30e-6	0.3	12e-6	1 – 0.03

As stated previously in Section 2.2.1, the developed TO procedure is employed to minimize structural compliance with a volume constraint. A prescribed volume fraction  $\varphi = 40\%$  is selected for the default volume constraint value, and each optimization is started with an initial uniform distribution  $\mathbf{x}_0 = 0.4$ . Further, stopping criteria are used to terminate the optimization process and these are defined in Eq. (51). The optimized result is considered to be converged when the maximum change of every design variable is below 0.01 (Andreassen et al., 2011). In addition, a fixed maximum of 1000 iterations ( $N_{iter}$ ) is added to limit the runtime for slow or not converging solutions.

$$\text{Stopping criteria} := \begin{cases} \max(\text{abs}(x_e^{i-1} - x_e^i)) < 0.01 & \forall x_e \in \mathbf{x} & \text{converged} \\ N_{iter} = 1000 & & \text{not converged} \end{cases} \quad (51)$$

The SIMP interpolation scheme is used with a penalization factor  $p = 3$  for all material properties  $(E, \kappa, \beta)$ . Furthermore, density filtering is used with a filter radius  $r_{min} = 3$ . The sensitivities obtained in Section 2.2.3 are modified in order to take into account the filtering (Andreassen et al., 2011).

In order to avoid convergence issues, the objective and corresponding sensitivities are divided by a scale factor  $\gamma_c = c_0/c^*$ , to limit the range of values to the acceptable bounds of  $[1,100]$  as stated by Svanberg (2007). The scale factor is determined based on the compliance value in the first iteration (denoted  $c_0$ ) and a scaled objective value  $c^* = 10$ , which is arbitrarily chosen within the aforementioned range. Throughout the optimization process, the scale factor remains constant. This ensures that the values for the objective and sensitivities are properly scaled regardless of the load level.

The optimization procedure with the default parameter values converged after 299 iterations and the optimized result is illustrated in Figure 5 with indication of both material phases. At the bottom, a large zone of insulation material appears, limiting the propagation of thermal energy into the structure on the top, which resembles a cellular beam. At the location of the support a thin strut from intermediate material appears, which is merely a result of the localized support conditions. The connection between the upper structure and the support at the right side of the domain remains thin due to the assumption of linear elasticity and the thermal loading at the location of the support.



Figure 5: Optimized result for default parameter values:  $T_f = 800^\circ\text{C}$ ,  $F_m = 10\text{kN}$ ,  $t = 10\text{mm}$

## 4.2 Influence of sensitivity analysis

In comparison with other approaches for the sensitivity analysis considering thermo-mechanical loading (Gao & Zhang, 2010; Gonçalves et al., 2022; Xia & Wang, 2008), in this paper the influence of the design variables on the thermal stiffness matrix and the temperature field is taken into account in the third term of Eq. (37). Since it is computationally expensive to compute the implicit derivative  $d\mathbf{T}/d\mathbf{x}$  (Zhu et al., 2019), often this term is neglected, i.e.  $\boldsymbol{\mu} = \mathbf{0}$  in Eq. (35). This results in only partial assessment of the sensitivities compared to the proposed sensitivities. Moreover, the sensitivity analysis in this study allows for a more efficient implementation, as the adjoint system  $\boldsymbol{\mu}$  (of size  $N$ ) needs to be solved only once each iteration. The efficiency is increased by defining the transformation matrices  $\mathbf{T}_T$  and  $\mathbf{T}_{TM}$  to speed up the calculation of the explicit derivative  $\partial\mathbf{F}/\partial\mathbf{T}$  in Eq. (50). A comparison of the optimized results for both approaches is made in Figure 6 for default parameter values and the corresponding compliance-volume plots are provided in Figure 7.

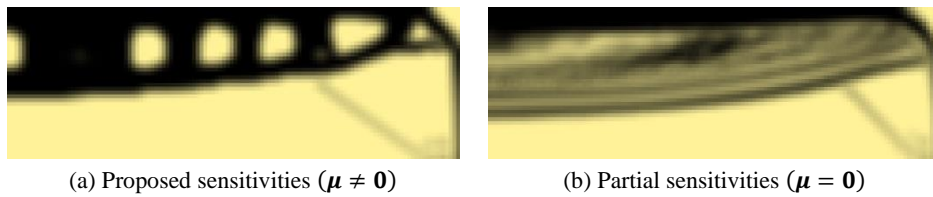


Figure 6: Optimized results for different sensitivities

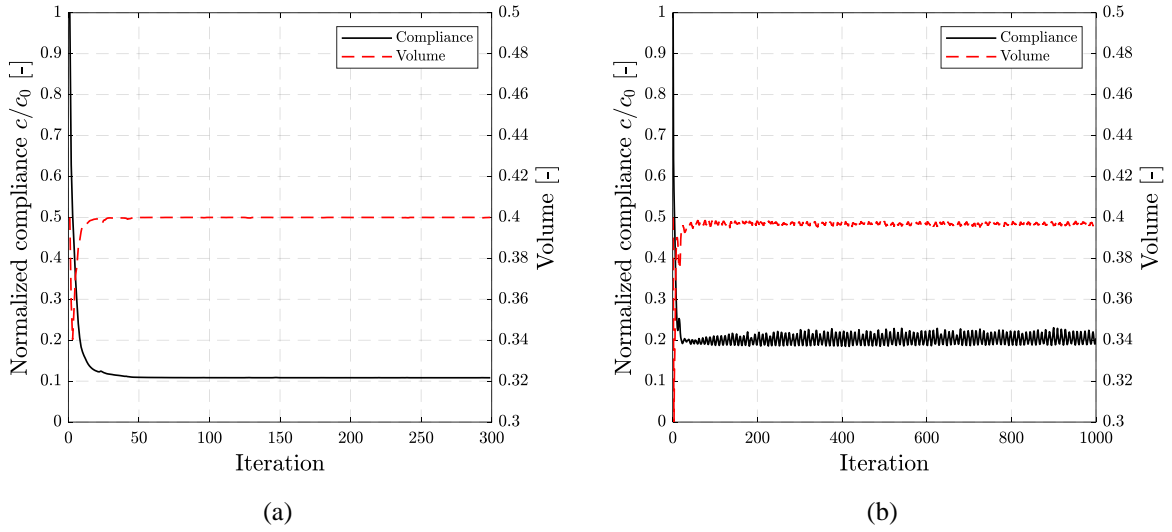


Figure 7: Normalized compliance and volume for (a) proposed sensitivity analysis, (b) partial sensitivity analysis

The final compliance in case of the proposed sensitivity analysis is  $122252.51 \text{ Nmm}$  after 299 iterations, whereas the optimized result using the partial sensitivities at iteration 1000, i.e. the solution did not converge, leads to a significantly larger compliance of  $231320.81 \text{ Nmm}$ . Moreover, the solution oscillates during the entire optimization process and the final volume is 0.3975, slightly below the imposed volume constraint. This observation is further confirmed by verification of the analytical partial sensitivities, as described in Appendix 1. The relative difference plots for different thermal gradients are provided in Figure 8.

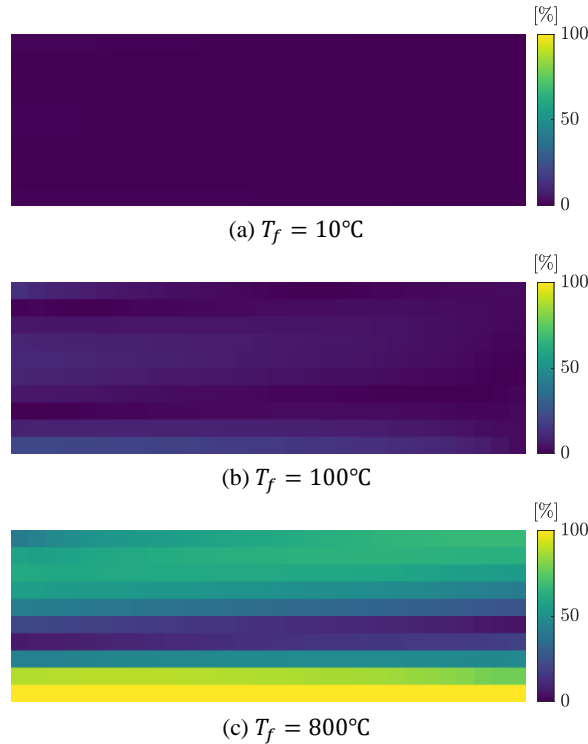


Figure 8: Relative differences for the partial sensitivities and different thermal gradients

For small thermal gradients, the contribution of the thermal load is negligible compared to the mechanical equivalent (see Section 4.3). Therefore, the sensitivity information in the third term in Eq. (37) is insignificant. However, in case of large thermal gradients, it is clear that the simplified approach with partial sensitivities does

not capture the sensitivity of the compliance properly, and leads to convergence issues and suboptimal results. Therefore it is advised to use the proposed sensitivity analysis when large thermal gradients are considered.

### 4.3 Influence of thermo-mechanical load ratio

Several studies have observed that the results of a TO procedure involving thermo-mechanical loads or thermo-elastic structures are dependent on the ratio between the thermal and mechanical loading (Cho & Choi, 2005; Deaton & Grandhi, 2013). In this paper, the thermo-mechanical load ratio (TMLR) is defined as a measure that accounts for how much of the structural compliance is caused by either mechanical or thermal actions on the structure. The latter is mechanically imposed on the structure due to (internally) restrained thermal expansion through the thermo-mechanical load vector, as discussed in Section 2.1.3. In Eq. (52), the TMLR, denoted symbolically as  $\eta$ , is expressed as the ratio between the thermal contribution to the compliance objective  $c_{th}$  and the total thermo-mechanical compliance  $c_{tot}$  for a solid design ( $\boldsymbol{x} = 1$ ).

$$\eta = \frac{c_{th}}{c_{tot}} = 1 - \frac{c_m}{c_{tot}} \quad (52)$$

where  $c_{th} = \boldsymbol{F}_{th}^T \boldsymbol{U}$  and  $c_{tot} = \boldsymbol{F}^T \boldsymbol{U}$  with  $\boldsymbol{U}$  the global displacement vector resulting from the combined thermo-mechanical action. Note that  $c_{tot} = c_m + c_{th}$  is valid based on Eq. (12) and therefore, the TMLR can be expressed in terms of the mechanical contribution  $c_m = \boldsymbol{F}_m^T \boldsymbol{U}$  as well.

As a result, the TMLR quantitatively represents the relative contribution of the thermal loading to the total compliance objective with  $0 \leq \eta \leq 1$ . When  $\eta = 0$  the total compliance value is entirely caused by the mechanical loading, in case  $\eta = 1$  the thermal loading is dominant instead, and for intermediate values both the thermal and mechanical actions are responsible for a part of the global deformation.

Note that the TMLR differs significantly depending on the material distribution, as indicated in Table 2 considering the default problem from Section 4.1, i.e.  $F_m = 10kN$  and  $T_f = 800^\circ C$ . In addition, the evolution of the TMLR and the volume during the optimization process is illustrated in Figure 9. The TMLR is calculated with Eq. (52) where  $c_{tot}$  is recalculated for each iteration based on the current material distribution to show the difference. The first value in the series is the TMLR for a solid design ( $\boldsymbol{x} = 1$ ) as a reference.

Table 2: Comparison for compliance and TMLR for solid, initial and optimized material layout

Material distribution	$c_{tot}$ [Nmm]	$c_{th}$ [Nmm]	$c_m$ [Nmm]	$\eta$ [-]
Solid ( $\boldsymbol{x} = 1$ )	12800211.38	12712800.91	87410.47	0.9932
Initial ( $\boldsymbol{x} = 0.4$ )	1129267.35	885423.52	243843.83	0.7841
Optimized ( $\boldsymbol{x} = \boldsymbol{x}_{opt}$ )	122252.51	28016.71	94235.80	0.2292

For a solid design ( $\boldsymbol{x} = 1$ ) the problem seems to be thermally dominant, as the thermal loading contributes for more than 99% to the structural compliance and the mechanical load is responsible for less than 1%. However, the TMLR changes drastically during the optimization, such that the mechanical load contributes for approximately 77% of the total compliance of the optimized structure ( $\boldsymbol{x} = \boldsymbol{x}_{opt}$ ), suggesting a mechanically dominant loading. Moreover, for an initial design equal to the prescribed volume fraction, e.g.  $\boldsymbol{x} = 0.4$ , the thermo-mechanical response of the structure is already influenced by the design-dependent thermal conductivity (see Table 2). Since the optimization is used to reduce the amount of material in an otherwise solid structure, the TMLR is calculated for a solid design in the next sections.

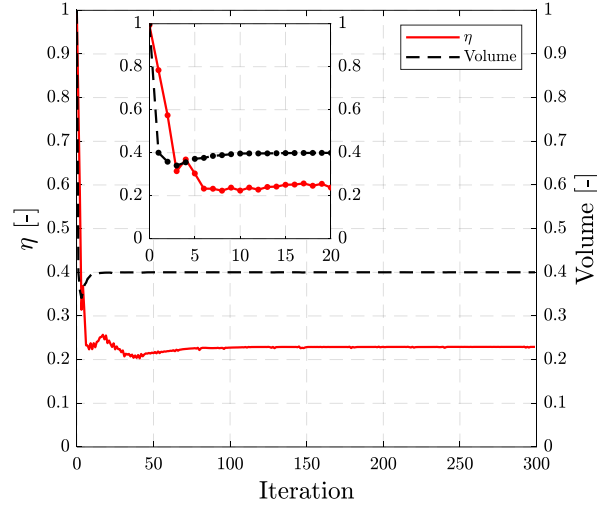


Figure 9: Evolution of the TMLR during optimization with a detailed plot showing the first 20 iterations

Generally, there are two strategies for investigating the effect of the TMLR: by changing either the variable thermal BCs/loading or the variable mechanical load. In the first strategy, the value of  $T_f$  is changed in order to impose a different thermal gradient on the structure to be optimized for, while in the second strategy the mechanical load  $F_m$  is varied to change the TMLR. By increasing either type of loading, the TMLR changes from being mechanically dominant ( $\eta < 0.5$ ) to thermally dominant ( $\eta > 0.5$ ) and vice versa, with a balanced ratio at  $\eta = 0.5$ . Even though the second strategy might cause an unrealistic response of the structure in case of high mechanical loads, i.e. excessive deformation beyond elastic or plastic limits, the effect of changing this parameter still provides valuable insight with regard to the TMLR.

In addition to the above mentioned strategies, another way of indirectly influencing the TMLR is by changing the out-of-plane thickness  $t$ . This parameter appears in the definitions of the coefficient matrices  $\mathbf{K}$  and  $\mathbf{K}_{th}$  and in the thermo-mechanical load vector  $\mathbf{F}_{th}$  as well. The mechanical response of a structure is not influenced by a varying thickness in case of a constant thermal gradient; the deformation remains constant regardless of the out-of-plane thickness. However, this is not the case when a mechanical load is considered as well. If the thickness increases, the stiffness increases as well and the structure will deform less when subjected to the same mechanical load. Therefore, considering a constant thermo-mechanical load, a thinner structure will be more mechanically dominant than a thicker structure.

The results for a varying TMLR are generated for different sets of parameters in the previously mentioned strategies in the following sections. The definition of  $\eta$  allows for the comparison of results for different load scenarios with similar TMLR values (see Section 4.3.4). The TMLR is calculated for each load case for a solid design ( $\mathbf{x} = 1$ ) for a proper evaluation of the thermal and mechanical contribution in a pre-optimized design.

### 4.3.1 Thermal gradient

In the first case, the thermal gradient is varied by changing the bottom surface temperature  $T_f$ , ranging from 0°C to 800°C, with a constant mechanical load of 10kN. The results for different thermal load cases are presented in Figure 10, accompanied by their corresponding TMLR.

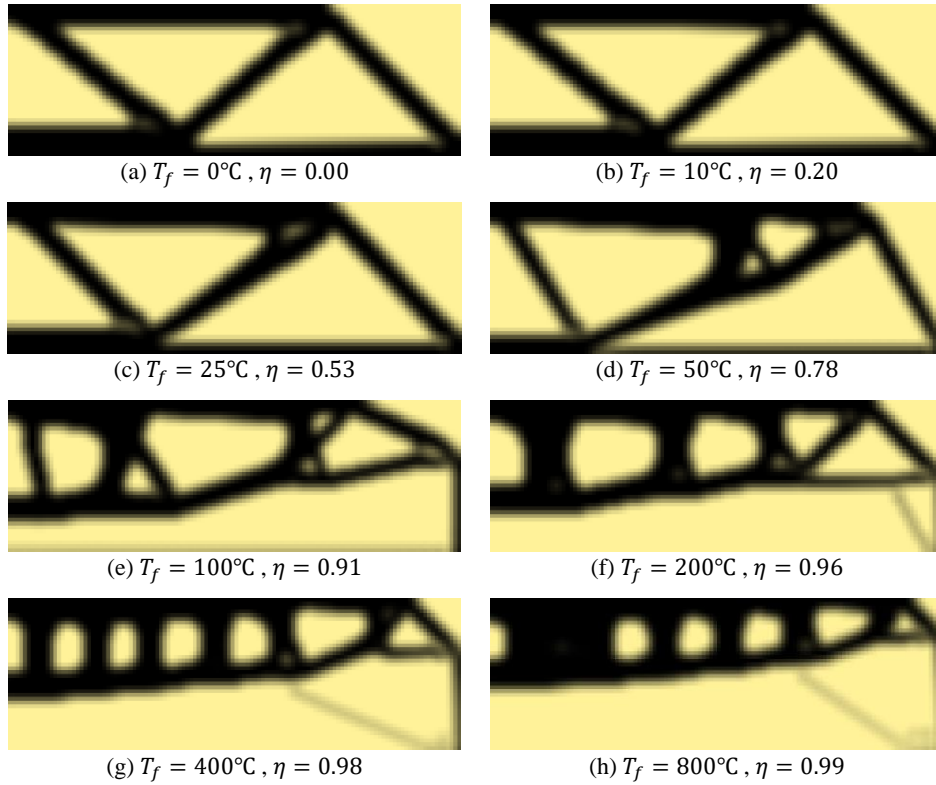


Figure 10: Optimized results for different thermal gradients

In Figure 10, cases (a) and (b) show similarities with the optimized solution for the mechanically only loaded MBB beam, as the TMLR is quite low with 0 and 0.2 respectively. Further increasing the bottom surface temperature also increases the TMLR and the associated contribution of the thermal loads to the compliance. The truss-like structure gradually transforms into a cellular beam with a large insulation zone underneath.

The compliance history is plotted in Figure 11. Herein, a more detailed plot indicates the fast convergence rate, as the final compliance value is practically attained after 100 iterations for most load cases.

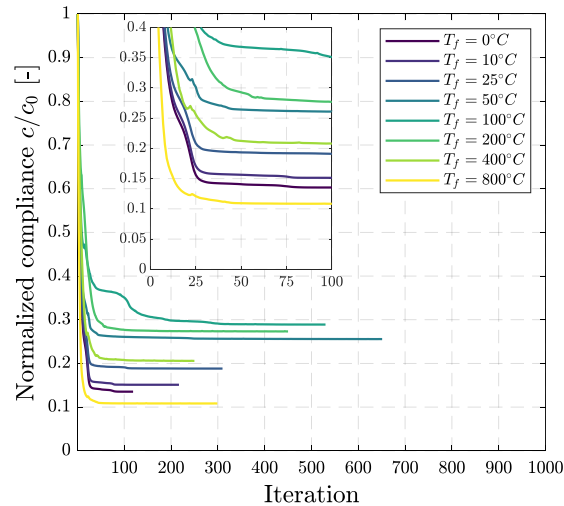


Figure 11: Normalized compliance evolution for different thermal gradients

### 4.3.2 Mechanical load

In this section the thermal gradient remains constant with  $T_f = 800^\circ\text{C}$  and the mechanical load  $F_m$  is varied, ranging from  $0\text{kN}$  to  $1000\text{kN}$ . The results for different mechanical load cases are presented in Figure 12, accompanied by their corresponding TMLR and final volume  $V_f$ .

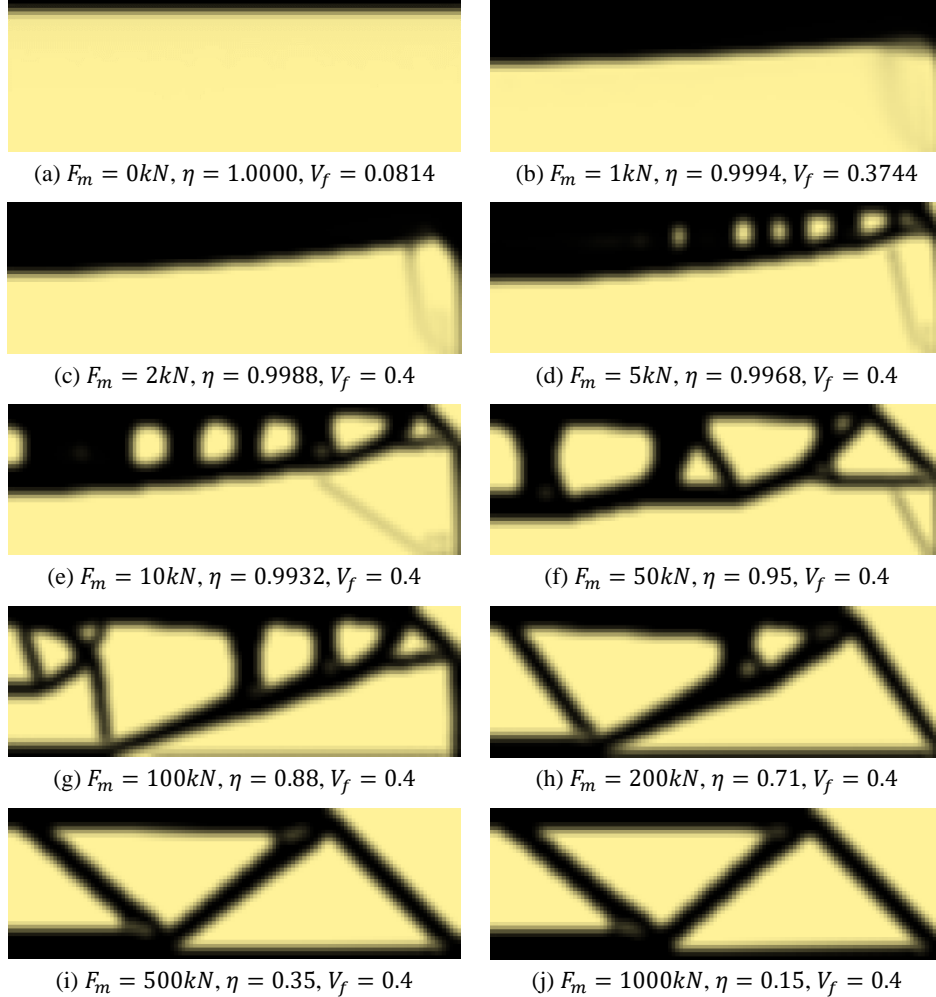


Figure 12: Optimized results for different mechanical loads

Similar to the results of the varying thermal gradient, the optimized topology is significantly different for various mechanical loads and TMLR values. In absence of mechanical loads in case (a) or for very low values of  $F_m$  in case (b), the final volume  $V_f$  is lower than the prescribed volume fraction. Further increasing the mechanical load to case (c) and onwards, the volume constraint is active again (see Section 4.4). Between case (h) and case (i) the problem changes from thermally to mechanically dominant and resembles the solution for a purely mechanically loaded MBB beam.

The compliance history is plotted in Figure 13. Herein, a more detailed plot indicates the fast convergence rate, as the final compliance value is again practically attained after 100 iterations for most mechanical load cases.

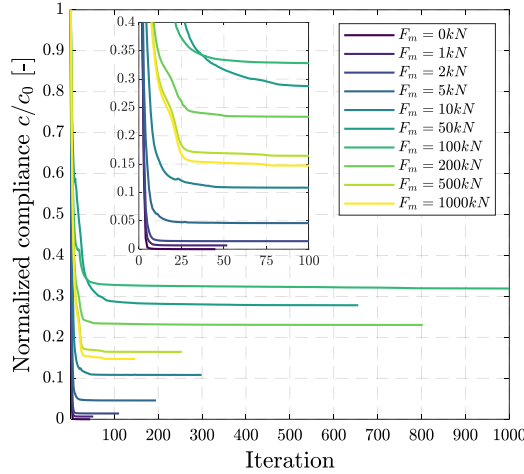


Figure 13: Normalized compliance evolution for different mechanical loads

### 4.3.3 Out-of-plane thickness

The third influential parameter for the TMLR is the out-of-plane thickness  $t$ , which is varied to  $1\text{ mm}$  and  $100\text{ mm}$ . The results are provided in Figure 14.



(a)  $t = 1\text{ mm}$ ,  $\eta = 0.9988$



(b)  $t = 100\text{mm}$ ,  $\eta = 0.9994$

Figure 14: Optimized results for different out-of-plane thicknesses

As a result, changing the thickness is inversely proportional to changing the total mechanical load. Moreover, the result in case (a) for one tenth of the default thickness ( $1\text{ mm}$ ) is exactly the same as the result for a tenfold mechanical load ( $100\text{ kN}$ ), considering a constant thermal load.

A second indirect conclusion is the fact that the results considering a realistic thickness (for concrete structures) and realistic thermo-mechanical loading are prominently thermally dominant, assuming steady-state heat conduction.

### 4.3.4 Comparison of the thermo-mechanical load ratio

As mentioned previously, the quantitative definition of the TMLR in Eq. (52) allows for a comparison of 2 different thermo-mechanical load cases that share the same TMLR. As such, two load cases are compared in Figure 15.



(a)  $T_f = 100^\circ\text{C}$ ,  $F_m = 10\text{kN}$ ,  $t = 10\text{mm}$ ,  $\eta = 0.91$     (b)  $T_f = 800^\circ\text{C}$ ,  $F_m = 80\text{kN}$ ,  $t = 10\text{mm}$ ,  $\eta = 0.91$

Figure 15: Comparison optimized results for equal TMLR

Unsurprisingly, as the TMLR is equal in both load cases, the optimized topology is exactly the same, despite the obvious difference in compliance value. Scaling the thermal and mechanical load equally, the TMLR remains constant. Similar results can be obtained by changing the thickness according to Section 4.3.3. Evidently, this result is only true in case the material properties are independent of the temperature.

## 4.4 Influence of volume constraint

The results for the varying mechanical load already revealed that the volume constraint becomes inactive when the problem is thermally dominant. A similar observation was made by Gao and Zhang (2010). Therefore, in this section the effect of the volume constraint on the optimized results is briefly investigated. The volume fraction  $\varphi$  is changed, ranging from 0.1 to 1, for the set of thermal gradients discussed in Section 4.3.1. The corresponding final volume fractions  $V_f$  are reported in Figure 16 in function of the imposed volume constraint.

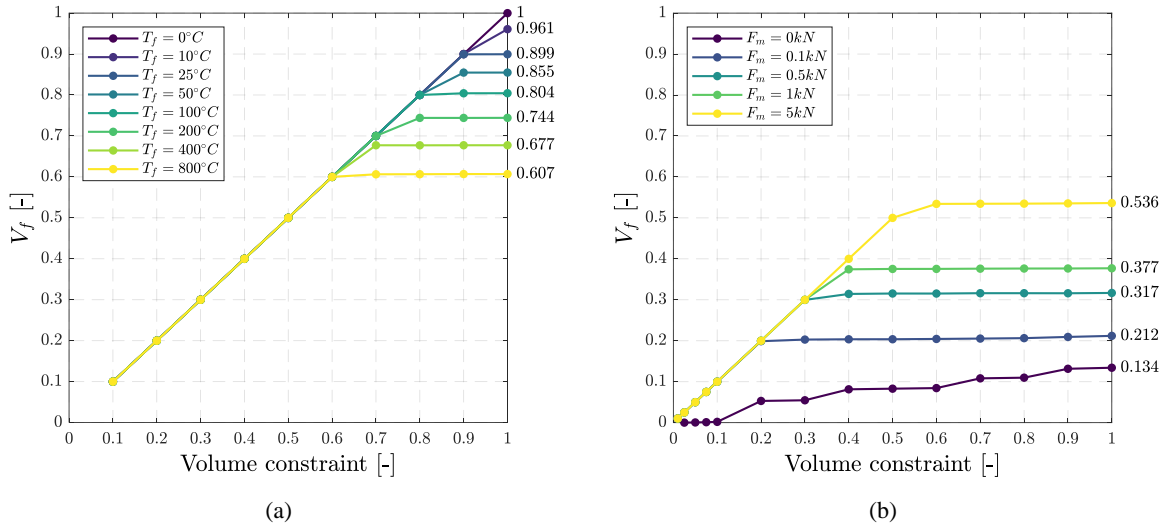


Figure 16: Final volume in function of volume constraint for (a) different thermal gradients and (b) low mechanical loads

The results in Figure 16a show that the inactivity of the volume constraint is dependent on the thermal gradient, and more specifically on the TMLR. For an increasing thermal gradient, the problem becomes thermally more dominant and the final volume of the optimized structure is restricted to a smaller fraction of the initial design domain than prescribed.

Similarly, the volume constraint becomes inactive for very low mechanical load levels, as illustrated in Figure 16b. Intuitively, in absence of a mechanical load ( $F_m = 0\text{kN}$ ) a void structure would be expected in order to minimize the thermally induced loads and consequently reduce compliance to a global minimum. The remaining solid and intermediate density elements on top of the design domain (e.g. in Figure 12a) can be attributed to the use of the MMA solver and the fact that the design space is nonconvex, which unavoidably may lead to local (and potentially suboptimal) solutions.

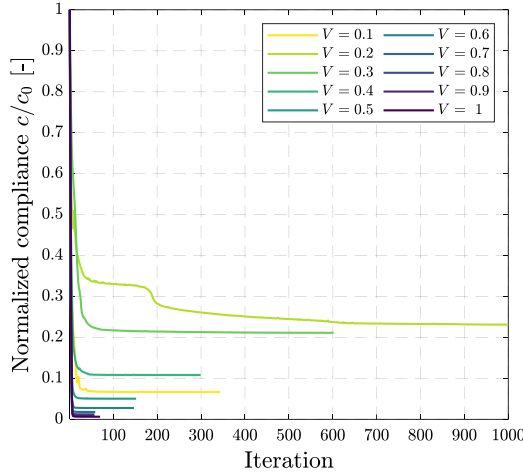


Figure 17: Normalized compliance evolution for different volume constraints

Apart from the difference in TMLR, the volume constraint itself affects the optimization, as illustrated in Figure 17. For low volume constraints (below 0.4 in this case), the optimization process is more often faced with a slower convergence rate. Nevertheless, even for cases with slow convergence (e.g.  $V = 0.2$ ), the compliance appears to monotonously decrease without oscillations as the optimization process continues.

Potential remedies to overcome convergence issues and local suboptimal solutions are the use of more advanced solvers such as GCMMA or GBMMA and modified interpolation schemes, as discussed by Bruyneel & Duysinx (2005). Additionally, other stopping or convergence criteria can be considered as well.

## 4.5 Influence of material interpolation

In this section the influence of the material interpolation is investigated, where the penalization factors for the thermal conductivity are varied. Although several studies have used the RAMP interpolation scheme (Deaton & Grandhi, 2013; Gao & Zhang, 2010; Zhu et al., 2019) before to improve convergence, in this study the SIMP method is employed as it did not lead to the reported numerical issues. The aim is to provide a preliminary insight into how the material interpolation scheme influences the results; it is not an extensive parameter study on the penalization factors. The different penalization schemes are listed in Table 3 and illustrated in Figure 18.

Table 3: Different material penalization schemes

Identifier	$E(x_e)$	$\kappa(x_e)$	$\beta(x_e)$
SIMP 3-3-3	$p_E = 3$	$p_\kappa = 3$	$p_\beta = 3$
SIMP 3-1-3	$p_E = 3$	$p_\kappa = 1$	$p_\beta = 3$
SIMP 3-0.5-3	$p_E = 3$	$p_\kappa = 0.5$	$p_\beta = 3$

As indicated in Figure 18, for a larger penalization factor, the elements with the corresponding penalized values will appear to be a much better thermal insulator compared to a less penalized value. The penalization of the thermal conductivity is changed to 1 and 0.5 to deliberately influence result. For example, with a penalization factor below 1, the intermediate elements will be more conductive relative to their density and seem less efficient from a thermal perspective.

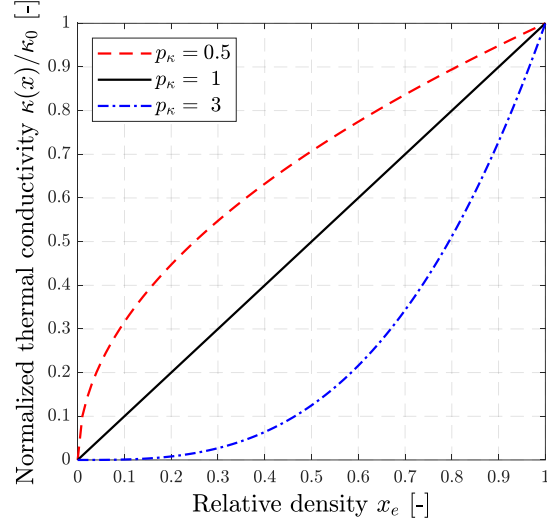
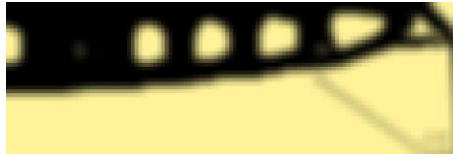


Figure 18: Thermal conductivity penalization schemes

The optimized results for the different penalization schemes are provided in Figure 19. By changing the penalization of the thermal conductivity, the overall shape of the optimized result is similar to the default penalization scheme. However, more intermediate material remains in the optimized result, which contradicts the thermal inefficiency of the intermediate material as stated above.



(a)  $T_f = 800^\circ\text{C}$ ,  $F_m = 10\text{kN}$ , SIMP 3-3-3,  $c = 122252.51\text{ Nmm}$



(b)  $T_f = 800^\circ\text{C}$ ,  $F_m = 10\text{kN}$ , SIMP 3-1-3,  $c = 115711.74\text{ Nmm}$



(c)  $T_f = 800^\circ\text{C}$ ,  $F_m = 10\text{kN}$ , SIMP 3-0.5-3,  $c = 112348.65\text{ Nmm}$

Figure 19: Optimized results for different penalization schemes

## 4.6 Performance

One of the objectives of this study is the development of a compact and efficient MATLAB code for topology optimization with thermo-mechanical loads, inspired by the popular 88-line code by Andreassen et al. (2011). Therefore, a brief section is dedicated to the performance.

In order to quantitatively describe the efficiency of the code, 3 different meshes are applied to the numerical problem with default parameters, as discussed in Section 4.1. The results were generated on a Dell Precision 3530 laptop with an Intel® Core™ i7-8850H processor with 16GB memory running MATLAB R2021b on Windows 10 Enterprise.

The optimization is carried out for a mesh of  $120 \times 40$ ,  $300 \times 100$  and  $600 \times 200$  elements, i.e. with an edge length of 10, 4 and 2 mm, with adjusted filter radius  $r_{min}$  equal to 3, 7.5 and 15 respectively. The average iteration times for these cases are listed in Table 4.

Table 4: Iteration time in seconds for different mesh sizes

Mesh	$120 \times 40$	$300 \times 100$	$600 \times 200$
Iteration time [s]	0.11	0.81	3.83

The results clearly show the fast iteration time for each of the mesh sizes, especially considering the solution of three linear systems per iteration, i.e. two for the thermo-mechanical analysis and one additional system for the sensitivity analysis. Additionally, the developed code is able to run optimizations with +1M elements and an iteration time under a minute, however, this is in part limited by the applied filter, as the band width of the filter matrix (and associated memory) increases for a larger filter radius. Alternative filters, such as the Heaviside projection filter, are discussed by Andreassen et al. (2011).

## Discussion

In this study, an efficient compliance-based topology optimization procedure is developed for structures subjected to thermo-mechanical loads considering steady-state heat conduction and weak thermo-mechanical coupling. Herein, a number of assumptions were made, both in the thermo-mechanical model and the optimization procedures. In the following, some remarks with regard to these assumptions are briefly discussed, as well as the identified research needs.

The numerical modelling of the structural behavior of components in the construction industry is dependent on the material properties. In this work, the assumption is made that the material behaves linearly elastic. This is a crude simplification for common construction materials, such as concrete, where more realistically an elastoplastic model involving damage evolution is used. Furthermore, the material properties are not temperature-dependent, even though large thermal gradients cause a significant change in these properties. In addition, no physical degradation of the insulation material is considered. Nevertheless, the influence of the TMLR on the results, as reported in this study, will still be relevant when more advanced material models are considered.

The Dirichlet conditions in the thermal analysis remain constant during the optimization. This directly influences the results and leads to a layer of insulation material at the location of the applied boundary condition in case of thermally dominant problems. This issue can be resolved by iteratively updating the thermal boundary during the optimization, similar to the design optimization with pressure loads (Hammer & Olhoff, 2000). Furthermore, only heat conduction is considered and extending this to include (internal) convection and (cavity) radiation seems the logical next step to avoid the use of a solid insulation material in the voids.

As mentioned previously, the design of structural components involves checking various requirements. In this work only stiffness is considered, despite other studies disproving of this objective for structural design with thermo-mechanical loads (Deaton & Grandhi, 2013; Pedersen & Pedersen, 2012), based on the volume constraint not being active and lack of optimization of the structural strength. However, stiffness is an important aspect of structural components in the construction industry, hence it makes sense to take this into account and study how the optimization is influenced. The other structural requirements can be added in future extensions, although the design of concrete structures entails additional challenging aspects as mentioned above.

## Conclusions

In this paper, an efficient topology optimization procedure with thermo-mechanical loads considering steady-state heat conduction is presented. The adjoint method is employed to determine the analytical sensitivities, which contain the complete influence of the design variables on the compliance objective. A compact and easy to understand 138-line MATLAB code is developed and specific parts of the code are discussed in more detail. The code is made available in the supplementary material as a starting point for further research.

The numerical example of an MBB beam, extended with thermal loading, is used to show the influence of several parameters related to the thermo-mechanical loading. The proposed sensitivities are verified and compared to partial sensitivities in which the influence on the thermal stiffness matrix and temperature is neglected. As a result, in case of large thermal gradients, the partial sensitivities are not able to capture the complete influence of the thermal loading, and therefore it is advised to consider the proposed sensitivities for further research. Subsequently, an expression for the thermo-mechanical load ratio (TMLR) is presented as a quantitative measure to compare optimized results with equivalent TMLRs. The influence of the TMLR is investigated based on various load scenarios involving different thermal gradients and mechanical loads and by changing the out-of-plane thickness. Overall, it can be concluded that the optimized results are highly dependent on the TMLR. Furthermore, it is shown that the imposed volume constraint becomes inactive depending on the TMLR and that the penalization of the thermal conductivity influences the occurrence of intermediate densities in the final solution.

Further research will look into applying the same approach in case of transient heat conduction and considering temperature-dependent material properties.

## Appendices

### Appendix 1: Verification sensitivity analysis

The verification of the analytical sensitivities obtained with the adjoint sensitivity analysis (Section 2.2.3) is performed based on the example of the MBB beam in Section 4. The analytical sensitivities of several arbitrary elements are compared with their corresponding numerical equivalent values, which are calculated with a central finite difference scheme (Cho & Choi, 2005), as expressed in Eq. (53).

$$\frac{\Delta c}{2\Delta x_i} = \frac{c(x_i + \Delta x_i) - c(x_i - \Delta x_i)}{2\Delta x_i} \quad (53)$$

with  $c$  the structural compliance,  $\Delta x_i$  a small perturbation of the element density of  $\mathcal{O}(10^{-8})$  and  $x_i$  the relative density of element  $i$ .

The relative (mean) difference between the analytical  $dc/dx_i$  and numerical sensitivities  $\Delta c/2\Delta x_i$ , denoted  $\overline{\delta c}$  here, is determined with Eq. (54), adapted from Tang et al. (2019).

$$\overline{\delta c} = \frac{\left| \frac{\Delta c}{2\Delta x_i} - \frac{dc}{dx_i} \right|}{\left| \frac{dc}{dx} \right|} \times 100\% \quad (54)$$

with  $\overline{|dc/dx|}$  the mean value of the analytical sensitivities of all elements.

A comparison of the sensitivities is made on a coarser mesh of  $10 \times 30$  elements for the sake of clarity. The sensitivities and corresponding differences of an arbitrary selection of 6 elements (indicated in Figure 20) is

provided in Table 5. The average iteration time considering the numerical sensitivities is 1.465 s, which is more than 200 times slower compared to 0.0064 s in case of the analytical sensitivities and clearly shows the advantage of the adjoint method for a high element count.

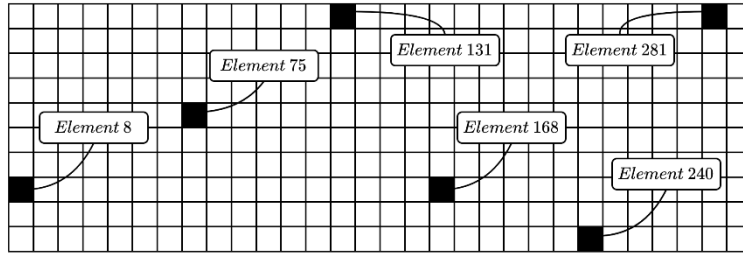


Figure 20: Mesh and element set for verification

The results in Table 5 show insignificant differences between the analytical and numerical sensitivities, which confirms the accuracy of the sensitivities and justifies the use of the adjoint method in the proposed TO procedure. In addition, the verification results are visually presented in Figure 21.

Table 5: Sensitivity analysis verification results

Element $i$	First iteration			Last iteration		
	$\frac{dc}{dx_i}$	$\frac{\Delta c}{\Delta 2x_i}$	$\overline{\delta c}$ [%]	$\frac{dc}{dx_i}$	$\frac{\Delta c}{\Delta 2x_i}$	$\overline{\delta c}$ [%]
8	35060.256878	35060.255779	4.22e-6	128.093491	128.073299	7.16e-4
75	3953.339069	3953.338095	3.74e-6	-6612.915554	-6612.925220	3.43e-4
131	-18723.527135	-18723.527861	2.79e-6	-6759.678493	-6759.676742	6.21e-5
168	41235.798354	41235.799892	5.90e-6	-0.000004	0.004647	1.65e-4
240	77244.383298	77244.384300	3.85e-6	-1.748712	-1.747126	5.62e-5
281	-12524.496129	-12524.495334	3.05e-6	-2885.642171	-2885.639044	1.11e-4

Note that using the mean value  $|\overline{dc/dx}|$  ensures a valid comparison for the large range of values, as in other formulations (Tang et al., 2019), the relative errors would become much larger in case of very small (but relatively very different) sensitivity values, e.g. elements 8, 168, 240 in Table 5.

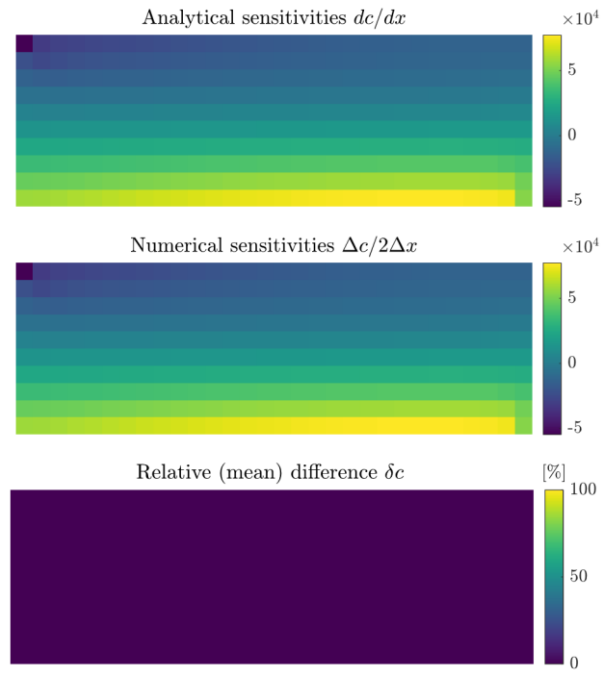


Figure 21: Sensitivity analysis verification

## Appendix 2: A 138-line MATLAB code for topology optimization with steady thermo-mechanical loads

```

1 %% A 138-line MATLAB code for topology optimization with steady thermo-mechanical loads %%
2 function top_tml_shc(L,h,t,z,Vf,rmin,pE,pk,pb)
3 addpath('C:\Users\...\MMA scripts\'); tic;
4 %% PARAMETERS
5 nelx = round(L/z); nely = round(h/z); nele = nelx*nely;
6 ini = Vf;
7 %% MATERIAL PROPERTIES
8 E0 = 30e3; Emin = 30e-6;
9 nu = 0.3;
10 k0 = 1; kmin = 0.03;
11 alpha = 12e-6;
12 Fth0 = E0*alpha*t*z/2/(1-nu);
13 %% PREPARE THERMAL FEA
14 TA1 = [ 8 -2; -2 8];
15 TA2 = [-4 -2; -2 -4];
16 KEth = t/12*[TA1 TA2; TA2 TA1];
17 Tnodenrs = reshape(1:(nely+1)*(nelx+1),nely+1,nelx+1);
18 TedofVec = reshape(Tnodenrs(1:end-1,1:end-1)+1,nele,1);
19 TedofMat = repmat(TedofVec,1,4)+repmat([0 nely+[1 0] -1],nele,1);
20 TiK = reshape(kron(TedofMat,ones(4,1))',16*nele,1);
21 TjK = reshape(kron(TedofMat,ones(1,4))',16*nele,1);
22 Tmaxdof = (nely+1)*(nelx+1);
23 % DEFINE LOADS AND SUPPORTS (HEATED BOTTOM EDGE)
24 T0 = 0; T1 = 800;
25 TT0 = T0*ones(Tmaxdof,1);
26 Q = sparse([],[],0,Tmaxdof,1);
27 T = ones(Tmaxdof,1)*T0;
28 TBC1 = 1:nely+1:Tmaxdof;
29 TBC2 = nely+1:nely+1:Tmaxdof;
30 T(TBC2) = T1;
31 Tcdofs = [TBC1 TBC2];
32 Tfdofs = setdiff(1:Tmaxdof,Tcdofs);
33 %% PREPARE MECHANICAL FEA
34 MA11 = [12 3 -6 -3; 3 12 3 0; -6 3 12 -3; -3 0 -3 12];
35 MA12 = [-6 -3 0 3; -3 -6 -3 -6; 0 -3 -6 3; 3 -6 3 -6];
36 MB11 = [-4 3 -2 9; 3 -4 -9 4; -2 -9 -4 -3; 9 4 -3 -4];
37 MB12 = [ 2 -3 4 -9; -3 2 9 -2; 4 9 2 3; -9 -2 3 2];
38 KE = t/(1-nu^2)/24*([MA11 MA12;MA12' MA11]+nu*[MB11 MB12;MB12' MB11]);
39 MedofVec = reshape(2*Tnodenrs(1:end-1,1:end-1)+1,nele,1);
40 MedofMat = repmat(MedofVec,1,8)+repmat([0 1 2*nely+[2 3 0 1] -2 -1],nele,1);
41 MiK = reshape(kron(MedofMat,ones(8,1))',64*nele,1);
42 MjK = reshape(kron(MedofMat,ones(1,8))',64*nele,1);
43 Mmaxdof = 2*(nely+1)*(nelx+1);
44 % DEFINE LOADS AND SUPPORTS (HALF MBB-BEAM)
45 Fm = sparse(2,1,-10000/2,Mmaxdof,1);
46 U = zeros(Mmaxdof,1);
47 Mcdofs = [Mmaxdof 1:2*nely+2+1];
48 Mfdofs = setdiff(1:Mmaxdof,Mcdofs);
49 %% PREPARE THERMO-MECHANICAL LOAD VECTOR AND ADJOINT VARIABLE
50 Itm = [-1 -1 1 -1 1 1 -1 1];
51 TT = sparse(repmat((1:nele)',1,4),TedofMat,1/4,nele,Tmaxdof);
52 TTM = sparse(repmat((1:nele)',1,8),MedofMat,repmat(Itm,nele,1),nele,Mmaxdof);
53 mu_adj = zeros(Tmaxdof,1);
54 %% PREPARE FILTER
55 iH = ones(nele*(2*(ceil(rmin)-1)+1)^2,1);
56 jH = ones(size(iH));
57 sH = zeros(size(iH));
58 i = 0;
59 for i1 = 1:nelx
60     for j1 = 1:nely
61         e1 = (i1-1)*nely+j1;
62         for i2 = max(i1-(ceil(rmin)-1),1):min(i1+(ceil(rmin)-1),nelx)
63             for j2 = max(j1-(ceil(rmin)-1),1):min(j1+(ceil(rmin)-1),nely)
64                 e2 = (i2-1)*nely+j2;
65                 i = i+1;
66                 iH(i) = e1;
67                 jH(i) = e2;
68                 sH(i) = max(0,rmin-sqrt((i1-i2)^2+(j1-j2)^2));
69             end
70         end
71     end

```

```

72 end
73 H = sparse(iH,jH,sH);
74 Hs = sum(H,2);
75 %% INITIALIZE ITERATION
76 xnew = ones(nely,nelx)*ini;
77 xold2 = xnew(:); xold1 = xnew(:); xval = xnew(:);
78 xmax = ones(nele,1); upp = xmax; xmin = zeros(nele,1); low = xmin;
79 iter = 0; change = 1;
80 %% START ITERATION
81 while change > 0.01 && iter < 1000
82     iter = iter + 1; time0 = toc;
83     % MATERIAL INTERPOLATION
84     Ex = Emin+xnew(:)'.^pE*(E0-Emin);
85     dEdx = pE*xnew(:)'.^(pE-1)*(E0-Emin);
86     kx = kmin+xnew(:)'.^pk*(k0-kmin);
87     dkdx = pk*xnew(:)'.^(pk-1)*(k0-kmin);
88     fx = Emin/E0+xnew(:)'.^pb*(1-Emin/E0);
89     dfdx = pb*xnew(:)'.^(pb-1)*(1-Emin/E0);
90     % THERMAL FEA
91     TsK = reshape(KEth(:)*kx,16*nele,1);
92     Kth = sparse(TiK,TjK,TsK); Kth = (Kth+Kth')/2;
93     T(Tfdofs) = Kth(Tfdofs,Tfdofs)\(Q(Tfdofs)-Kth(Tfdofs,Tcdofs)*T(Tcdofs));
94     % THERMO-MECHANICAL LOAD VECTOR
95     DT = TT*(T-TT0);
96     Fth = TTM'*(Fth0*fx'.*DT);
97     % MECHANICAL FEA
98     F = Fm + Fth;
99     MsK = reshape(KE(:)*Ex,64*nele,1);
100    K = sparse(MiK,MjK,MsK); K = (K+K')/2;
101    U(Mfdofs) = K(Mfdofs,Mfdofs)\F(Mfdofs);
102    % OBJECTIVE FUNCTION AND SENSITIVITY ANALYSIS
103    v = mean(xnew(:));
104    dv = ones(nele,1)/nele;
105    ce = sum((U(MedofMat)*KE).*U(MedofMat),2);
106    c = sum(Ex'.*ce);
107    dc1 = -dEdx'.*ce;
108    dc2 = 2*Fth0*(U(MedofMat)*Itm').*dfdx'.*DT;
109    Q_adj = (-2*U'*(TTM'.*(Fth0*fx))*TT)';
110    mu_adj(Tfdofs) = Kth(Tfdofs,Tfdofs)\Q_adj(Tfdofs);
111    dc3 = dkdx'.*(sum((mu_adj(TedofMat)*KEth)).*T(TedofMat),2));
112    dc = reshape(dc1+dc2+dc3,nely,nelx);
113    if iter == 1; c_scale = c/10; end
114    c = c/c_scale;
115    dc = dc/c_scale;
116    % FILTERING/MODIFICATION OF SENSITIVITIES
117    dc(:) = H*(dc(:))./Hs;
118    dv(:) = H*(dv(:))./Hs;
119    % MMA UPDATE OF DESIGN VARIABLES
120    m = 1; n = nele;
121    f0val = c; df0dx = dc(:);
122    fval = v/Vf-1; dfdx = dv(:)/Vf;
123    a0 = 1; a1 = zeros(m,1); c1 = 1000*ones(m,1); d1 = ones(m,1);
124    [xmma,~,~,~,~,~,~,~,low,upp] = ...
125    mmasub(m,n,iter,xval,xmin,xmax,xold1,xold2,f0val,df0dx,fval,dfdx,low,upp,a0,a1,c1,d1);
126    xold2 = xold1; xold1 = xval; xval = xmma;
127    change = max(abs(xval(:)-xold1(:)));
128    xnew = reshape(xmma,nely,nelx);
129    xnew(:) = (H*xnew(:))./Hs;
130    % PRINT RESULTS
131    fprintf([' I: %5i Obj: %12.2f Volume: %6.4f Change: %6.3f '...
132    ' IterTime: %7.2f TotalTime: %9.2f\n'],iter,(c*c_scale),v,change,toc-time0,toc);
133    % PLOT DESIGN VARIABLES
134    figure(1);
135    set(gcf,'position',[150 450 1200 400]);
136    imagesc(1-xnew);
137    colormap(gray); caxis([0 1]); axis equal; axis tight; axis off; drawnow;
138 end

```

### **Acknowledgements**

The authors thank Professor Krister Svanberg of the Royal Institute of Technology (KTH), Stockholm, for providing the MATLAB files for the MMA algorithm used in this study.

### **Funding**

This research was supported by Ghent University.

### **Replication of results**

The included results can be replicated with the developed MATLAB code in the supplementary material and executed by a command of the following form:

```
top_tml_shc(L,h,t,z,Vf,rmin,pE,pk,pb)
```

where the variables refer to the corresponding parameters discussed in the paper.

For example, the optimization with the default parameters can be solved by entering the following command:

```
top_tml_shc(1200,400,10,10,0.4,3,3,3,3)
```

The MATLAB files `mmasub.m` and `subsolv.m` for using the MMA algorithm are freely available on <http://www.smoptit.se/> under the GNU General Public License (GPLv3). One should reference them correctly in line 3 of the MATLAB code to carry out the optimization procedure.

### **Conflict of interest**

On behalf of all authors, the corresponding author states that there is no conflict of interest.

## References

- Allaire, G. (2015). A review of adjoint methods for sensitivity analysis, uncertainty quantification and optimization in numerical codes. *Ingénieurs de l'Automobile*, 836, 33–36. <https://hal.archives-ouvertes.fr/hal-01242950>
- Andreassen, E., Clausen, A., Schevenels, M., Lazarov, B. S., & Sigmund, O. (2011). Efficient topology optimization in MATLAB using 88 lines of code. *Structural Multidisciplinary Optimization*, 43(1), 1–16. <https://doi.org/10.1007/s00158-010-0594-7>
- Andrew, R. (2018). Global CO2 emissions from cement production, 1928–2017. *Earth Syst Sci Data*, 10, 195–217. <https://doi.org/10.5281/zenodo.831455>
- Bendsøe, M., & Sigmund, O. (2003). *Topology optimization: theory, methods and applications*. Springer. <https://doi.org/10.1007/978-3-662-05086-6>
- Bourdin, B., & Chambolle, A. (2003). Design-dependent loads in topology optimization. *ESAIM - Control, Optimisation and Calculus of Variations*, 9, 247–273. <https://doi.org/10.1051/COCV:2002070/>
- Bruyneel, M., & Duysinx, P. (2005). Note on topology optimization of continuum structures including self-weight. *Structural and Multidisciplinary Optimization*, 29(4), 245–246. <https://doi.org/10.1007/s00158-004-0484-y>
- Chen, B. C., & Kikuchi, N. (2001). Topology optimization with design-dependent loads. *Finite Elements in Analysis and Design*, 37(1), 57–70. [https://doi.org/10.1016/S0168-874X\(00\)00021-4](https://doi.org/10.1016/S0168-874X(00)00021-4)
- Chen, J., Zhao, Q., & Zhang, L. (2022). Multi-Material Topology Optimization of Thermo-Elastic Structures with Stress Constraint. *Mathematics 2022, Vol. 10, Page 1216*, 10(8), 1216. <https://doi.org/10.3390/MATH10081216>
- Chen, Y., Ye, L., Zhang, Y. X., & Yang, C. (2021). A multi-material topology optimization with temperature-dependent thermoelastic properties. *Engineering Optimization*, 54(12), 2140–2155. <https://doi.org/10.1080/0305215X.2021.1977291>
- Cho, S., & Choi, J. Y. (2005). Efficient topology optimization of thermo-elasticity problems using coupled field adjoint sensitivity analysis method. *Finite Elements in Analysis and Design*, 41(15), 1481–1495. <https://doi.org/10.1016/j.finel.2005.05.003>
- Deaton, J. D., & Grandhi, R. v. (2013). Stiffening of restrained thermal structures via topology optimization. *Structural and Multidisciplinary Optimization*, 48(4), 731–745. <https://doi.org/10.1007/s00158-013-0934-5>
- Deaton, J. D., & Grandhi, R. v. (2014). A survey of structural and multidisciplinary continuum topology optimization: Post 2000. *Structural and Multidisciplinary Optimization*, 49(1), 1–38. <https://doi.org/10.1007/s00158-013-0956-z>
- Diaz, A., & Benard, A. (2003). Topology optimization of heat-resistant structures. *ASME 2003 International Design Engineering Technical Conferences and Computers and Information in Engineering Conference*. <https://doi.org/10.1115/DETC2003/DAC-48769>
- Ganobjak, M., & Carstensen, J. (2019). Topology-optimized insulating facebrick with aerogel filling. *Journal of Physics: Conference Series*, 1343, 12195. <https://doi.org/10.1088/1742-6596/1343/1/012195>
- Gao, T., Xu, P., & Zhang, W. (2016). Topology optimization of thermo-elastic structures with multiple materials under mass constraint. *Computers & Structures*, 173, 150–160. <https://doi.org/10.1016/j.compstruc.2016.06.002>
- Gao, T., & Zhang, W. (2010). Topology optimization involving thermo-elastic stress loads. *Structural and Multidisciplinary Optimization*, 42(5), 725–738. <https://doi.org/10.1007/S00158-010-0527-5>
- Giraldo-Londoño, O., Mirabella, L., Dalloro, L., & Paulino, G. H. (2020). Multi-material thermomechanical topology optimization with applications to additive manufacturing: Design of main composite part and its support structure. *Computer Methods in Applied Mechanics and Engineering*, 363, 112812. <https://doi.org/10.1016/J.CMA.2019.112812>

- Gonçalves, M., Dias-de-Oliveira, J. A., & Valente, R. (2022). A new bidirectional algorithm for topology optimization of thermoelastic structural problems. *International Journal of Mechanics and Materials in Design*, 18(2), 309–325. <https://doi.org/10.1007/s10999-022-09591-z>
- Hammer, V. B., & Olhoff, N. (2000). Topology optimization of continuum structures subjected to pressure loading. *Structural and Multidisciplinary Optimization*, 19(2), 85–92. <https://doi.org/10.1007/S001580050088>
- Hou, J., Zhu, J.-H., & Li, Q. (2016). On the Topology Optimization of Elastic Supporting Structures under Thermomechanical Loads. *International Journal of Aerospace Engineering*. <https://doi.org/10.1155/2016/7372603>
- Huang, X., & Xie, Y. M. (2011). Evolutionary topology optimization of continuum structures including design-dependent self-weight loads. *Finite Elements in Analysis and Design*, 47(8), 942–948. <https://doi.org/10.1016/J.FINEL.2011.03.008>
- Leader, M. K. (2021). *Stress-Based Topology Optimization for Steady-State and Transient Thermoelastic Design* [PhD thesis].
- Lee, E., & Martins, J. R. R. A. (2012). Structural topology optimization with design-dependent pressure loads. *Computer Methods in Applied Mechanics and Engineering*, 233–236, 40–48. <https://doi.org/10.1016/j.cma.2012.04.007>
- Lewis, R. W., Nithiarasu, P., & Seetharamu, K. N. (2004). *Fundamentals of the Finite Element Method for Heat and Fluid Flow*. John Wiley & Sons, Ltd. <https://doi.org/10.1002/0470014164>
- Li, D., Zhang, X., Guan, Y., & Zhan, J. (2010). Topology optimization of thermo-mechanical continuum structure. *IEEE/ASME International Conference on Advanced Intelligent Mechatronics, AIM*, 403–408. <https://doi.org/10.1109/AIM.2010.5695845>
- Li, Q., Steven, G. P., & Xie, Y. M. (2001). Thermoelastic topology optimization for problems with varying temperature fields. *Journal of Thermal Stresses*, 24(4), 347–366. <https://doi.org/10.1080/01495730151078153>
- Logan, D. L. (2016). A First Course in the Finite Element Method Sixth Edition. In *Thomson*.
- Ooms, T., Vantghem, G., Thienpont, T., van Coile, R., & de Corte, W. (2022). Different approaches for topology optimization of building structures subjected to thermo-mechanical loads due to fire. *ACSMO 2022, Asian Congress of Structural and Multidisciplinary Optimization 2022, Proceedings*, 8. <https://acsmo2022.org/>
- Pedersen, P., & Pedersen, N. L. (2012). Interpolation/penalization applied for strength design of 3D thermoelastic structures. *Structural and Multidisciplinary Optimization*, 45(6), 773–786. <https://doi.org/10.1007/s00158-011-0755-3>
- Picelli, R., Neofytou, A., & Kim, H. A. (2019). Topology optimization for design-dependent hydrostatic pressure loading via the level-set method. *Structural and Multidisciplinary Optimization*, 60(4), 1313–1326. <https://doi.org/10.1007/S00158-019-02339-Y>
- Picelli, R., Vicente, W., & Pavanello, R. (2015). Bi-directional evolutionary structural optimization for design-dependent fluid pressure loading problems. *Engineering Optimization*, 47(10), 1324–1342. <https://doi.org/10.1080/0305215X.2014.963069>
- Reddy, J. N., & Gartling, D. K. (2010). The finite element method in heat transfer and fluid dynamics third edition. In *The Finite Element Method in Heat Transfer and Fluid Dynamics, Third Edition*.
- Rodrigues, H., & Fernandes, P. (1995). A material based model for topology optimization of thermoelastic structures. *International Journal for Numerical Methods in Engineering*, 38(12), 1951–1965. <https://doi.org/10.1002/NME.1620381202>
- Sigmund, O. (2007). Morphology-based black and white filters for topology optimization. *Structural and Multidisciplinary Optimization*, 33(4), 401–424. <https://doi.org/10.1007/s00158-006-0087-x>
- Stoiber, N., & Kromoser, B. (2021). Topology optimization in concrete construction: a systematic review on numerical and experimental investigations. *Structural and Multidisciplinary Optimization*, 64(4), 1725–1749. <https://doi.org/10.1007/S00158-021-03019-6>

- Stolpe, M., & Svanberg, K. (2001). An alternative interpolation scheme for minimum compliance topology optimization. *Structural and Multidisciplinary Optimization*, 22, 116–124. <https://doi.org/10.1007/s001580100129>
- Svanberg, K. (1987). The Method of Moving Asymptotes - a New Method for Structural Optimization. *International Journal for Numerical Methods in Engineering*, 24(2), 359–373. <https://doi.org/10.1002/nme.1620240207>
- Svanberg, K. (2007). *MMA and GCMMA-two methods for nonlinear optimization*. 1–15. <https://people.kth.se/~krille/gcmma07.pdf>
- Tang, L., Gao, T., Song, L., Meng, L., Zhang, C., & Zhang, W. (2019). Topology optimization of nonlinear heat conduction problems involving large temperature gradient. *Computer Methods in Applied Mechanics and Engineering*, 357, 112600. <https://doi.org/10.1016/j.cma.2019.112600>
- Tortorelli, D. A., & Michaleris, P. (1994). Design sensitivity analysis: Overview and review. *Inverse Problems in Engineering*, 1(1), 71–105. <https://doi.org/10.1080/174159794088027573>
- van den Hende, K., & van Paepegem, W. (2021). *Multi-materiaal topologie optimalisatie van structurele onderdelen onder thermomechanische belastingen* [MSc thesis, Ghent University]. <http://lib.ugent.be/catalog/rug01:003015034>
- Vantighem, G., Boel, V., Steeman, M., & de Corte, W. (2019). Multi-material topology optimization involving simultaneous structural and thermal analyses. *Structural and Multidisciplinary Optimization*, 59(3), 731–743. <https://doi.org/10.1007/s00158-018-2095-z>
- Vantighem, G., de Corte, W., Steeman, M., & Boel, V. (2019). Density-based topology optimization for 3D-printable building structures. *Structural and Multidisciplinary Optimization*, 60(6), 2391–2403. <https://doi.org/10.1007/s00158-019-02330-7>
- Welty, J., Rorrer, G. L., & Foster, D. G. (2014). *Fundamentals of momentum, heat, and mass transfer*. John Wiley & Sons.
- Xia, Q., & Wang, M. Y. (2008). Topology optimization of thermoelastic structures using level set method. *Computational Mechanics*, 42(6), 837–857. <https://doi.org/10.1007/s00466-008-0287-x>
- Zheng, B., Chang, C., & Gea, H. (2009). Topology optimization with design-dependent pressure loading. *Structural and Multidisciplinary Optimization*, 38(6), 535–543. <https://doi.org/10.1007/s00158-008-0317-5>
- Zhu, X., Zhao, C., Wang, X., Zhou, Y., Hu, P., & Ma, Z.-D. (2019). Temperature-constrained topology optimization of thermo-mechanical coupled problems. *Engineering Optimization*, 51(10), 1687–1709. <https://doi.org/10.1080/0305215X.2018.1554065>
- Zienkiewicz, O. C., Taylor, R. L., & Zhu, J. Z. (2013). *The finite element method: Its basis and fundamentals*. Butterworth-Heinemann.